

# Turbulent flow regimes behind a coastal cape in a stratified and rotating environment

M. G. Magaldi <sup>a</sup>, T. M. Özgökmen <sup>a</sup>, A. Griffa <sup>a,b</sup>,  
E. P. Chassignet <sup>c</sup>, M. Iskandarani <sup>a</sup>, H. Peters <sup>a</sup>

<sup>a</sup>*Rosenstiel School of Marine and Atmospheric Science/MPO, Univ. of Miami,  
4600 Rickenbacker Cswy, Miami, Florida, 33149-1098, USA*

<sup>b</sup>*Istituto di Scienze Marine,  
Consiglio Nazionale delle Ricerche, Sezione di Lerici,  
Forte Santa Teresa, I-19036, Pozzuolo di Lerici (SP), Italy*

<sup>c</sup>*Center for Ocean-Atmospheric Prediction Studies, Florida State University,  
200 RM Johnson Bldg, Tallahassee, Florida, 32306-4320, USA*

---

## Abstract

A numerical study aimed at investigating the roles of both the stratification and topographic slope in generation of turbulent coherent structures in the lee of capes is presented. We consider a steady barotropic current impinging on an obstacle in a rotating and linearly-stratified environment. The obstacle is a triangular prism and represents an idealized headland extending from the coast. Numerical experiments are conducted at constant Rossby number  $Ro = 0.06$ , varying the Burger number,  $Bu$ , and the obstacle slope,  $\alpha$ .

Flow regime diagrams in the  $Bu - \alpha$  space are determined. For  $Bu < 0.1$ , vertical movement over the obstacle is enhanced and a fully-attached regime with pronounced internal waves is established. For  $0.1 \leq Bu < 1$ , fluid parcels flow more around the obstacle than over it. Flow separation occurs and small tip eddies start to shed. For  $Bu \geq 1$ , tip eddies merge to form larger eddies in the lee of the cape. We find that previous laboratory results cannot be used for gentler slopes, since bottom flow regimes are strongly dependent on  $\alpha$  when  $Bu \geq 1$ .

The form drag coefficient exerted by the cape is at least two orders of magnitude larger than the one due to skin friction. It increases with increasing Burger numbers and decreasing slopes. When no separation occurs (low  $Bu$ ), the increase with decreasing slopes is the result of the mixing associated with hydraulic phenomena. For intermediate and high  $Bu$ , form drag coefficients reach larger values as a result of the boundary layer mixing associated with flow separation. We put forth an empirical parametrization of form drag in the  $Bu - \alpha$  space.

*Key words:* Cape; headland; eddy generation; modeling; form drag; mixing.

---

## 1 Introduction

Coastal circulation is influenced by the complex shape of the coastline. In particular, leeward eddies have been observed behind topographic features like prominent headlands and capes (e.g. Pattiaratchi et al., 1986; Farmer et al., 2002; McCabe et al., 2006). These eddies impact the physics of coastal systems and play a role in biological, ecological, and geological processes. Leeward eddies affect the dispersion of dissolved pollutants (Hayward and Mantyla, 1990; Doglioli et al., 2004b), floating organisms (Chiswell and Roemmich, 1998; Roughan et al., 2005; Rankin et al., 1994; Murdoch, 1989), nutrients (John and Pond, 1992) and sediments (Pingree, 1978; Bastos et al., 2002, 2003; Jones et al., 2006).

From a dynamical perspective, capes and headlands are important for the circulation because they are associated with enhanced mixing, drag and dissipation (Farmer et al., 2002; Pawlak et al., 2003). All the processes usually observed around capes, like current separation, formation of eddies and generation of lee waves, result in a drag force imparted on the larger scale coastal flows. Obstacles can decelerate flows in two distinct ways: via tangential stresses over the surface of contact (skin drag), or via pressure differences across the obstacle (form drag). Recent studies associate the efficiency of the extraction of energy from coastal flows more with the obstacle shape than with the viscous dissipation due to bottom boundary layer processes. Moum and Nash (2000) and Nash and Moum (2001) find that, on a 5 km long obstacle, form drag exceeds skin friction by a factor of 2-3. According to the observations across Knight Inlet, Klymak and Gregg (2001, 2004) show that the form drag due to internal waves accounts for approximately 67% of the total energy dissipation and appears to be the major energy sink. It is followed by the drag due to horizontal eddies, bottom friction and internal dissipation. In the numerical simulations of Puget Sound and of the Strait of Juan de Fuca, both Lavelle et al. (1988) and Foreman et al. (1995) are obliged to use bottom drag coefficients about 5-10 times larger than the commonly used value ( $3 \times 10^{-3}$ ) in order to match observations. It is thought that the form drag associated with the unresolved topographic features present in the area is the cause of the missing dissipation (Edwards et al., 2004).

Since ocean coastlines are usually tortuous, and coastal areas are full of submerged topographic features like sills, straits and banks, the understanding of the processes influencing the form drag remains a critical point in modeling the ocean circulation realistically. This problem is inherently linked to the understanding of the conditions under which different coastal flow regimes appear. The theoretical study by MacCready and Pawlak (2001) shows that the form drag associated with a headland is affected by lee waves and eddy formation. However since they consider a small cape ( $\sim 1$  km) in a strongly-

stratified tidal system, their analysis neglects the Earth’s rotation and their results cannot be applied to the cases with small Rossby numbers, namely for slower flows impinging on larger obstacles. Thus, it is not clear under which conditions different flow regimes appear when rotation and stratification are both important for the dynamics.

Understanding the factors affecting eddy formation is challenging because the dynamics of the processes involved are complex. Eddy generation is connected to the phenomenon of current separation occurring in presence of obstacles (Batchelor, 1967) and it can be explained in terms of adverse pressure gradients and boundary layer detachment (Schlichting and Gersten, 2003). The studies of homogeneous non-rotating flows usually consider a constant flow impinging on a columnar (non-sloping) cylinder. They show the dependence of the separation process on different non-dimensional parameters like the Reynolds number, defined as  $Re = UD/\nu$ , where  $\nu$  is the kinematic viscosity, while  $U$  and  $D$  are the characteristic velocity and the horizontal dimension, respectively (Batchelor, 1967). For  $40 < Re < 1000$  a periodic eddy shedding regime is established and, if  $f_s$  is the shedding frequency, the Strouhal number  $St = f_s D/U$  can be defined. In a homogeneous non-rotating flow,  $St$  is usually constant and equal to 0.21 (Kundu and Cohen, 2002). Even in complex stratified and rotating conditions reproducing flows past islands, the Strouhal number remains close to this value, being  $St = 0.23$  (Dong et al., 2007). For geophysical applications, Tomczak (1988) distinguishes between shallow and deep water dynamics, depending on whether the dominant role of friction in the system is played by lateral or vertical stresses. Following the same idea and using the turbulent vertical viscosity  $\nu_v^*$ , Wolanski et al. (1984) introduce the so-called island wake parameter  $P = (UH^2)/(\nu_v^* D)$ . In analogy to the Reynolds number, this parameter quantifies the importance of lateral advection relative to the vertical friction. Many studies show how  $P$  effectively controls the flow around atolls and islands (Wolanski et al., 1996; Lloyd et al., 2001; Stansby and Lloyd, 2001; Neill and Elliott, 2004). Since in shallow waters bottom friction can be dominant, Pingree and Maddock (1980) use the bottom drag coefficient  $C_D$  instead of  $\nu_v^*$ . In this case, the importance of lateral advection relative to bottom friction is quantified by so-called equivalent Reynolds number,  $Re_f = H/(C_D D)$ .  $Re_f$  effectively controls the flow (Pattiaratchi et al., 1986; Signell and Geyer, 1991; Doglioli et al., 2004a). For very small  $Re_f$ , when friction dominates, the flow tends to follow the obstacle without separating. At increasing  $Re_f$ , laminar separation occurs and attached stationary eddies form in the lee of the obstacle. For higher  $Re_f$ , the eddies detach and propagate downstream, leading to an eddy-shedding unstable regime.

If  $N$  is the buoyancy frequency and  $H$  the characteristic vertical scale, the importance of stratification is generally measured by the internal Froude number,  $Fr = U/(NH)$ . For  $0.2 < Fr < 1$  three-dimensional motions are present in

the wake of the obstacle and they are responsible for the generation of small-scale tip eddies. When stratification is sufficiently high,  $Fr < 0.2$ , vertical motions are suppressed and the flow field is almost two-dimensional (Davies et al., 1990a). Internal waves, as well as the vertical extent of the wake, are strongly reduced and vertically thin “pancake” vortices can emerge (Lin and Pao, 1979). When  $Fr \geq 1$  (supercritical flows), upstream propagation of internal gravity waves is not possible since the velocity of the fluid is equal or larger than their speed (Kundu and Cohen, 2002). Supercritical conditions and hydraulic jumps can then be encountered in presence of contractions and sills (Armi, 1986). For a two-layer system, the strength of the net barotropic flow changes the position of the critical point depending upon which the geometrical changes happen in width (Armi and Farmer, 1986) or in depth (Farmer and Armi, 1986). Pawlak and Armi (1996) and Pawlak and Armi (1997) extend these results to include the effects of friction.

If  $f$  is the Coriolis parameter, the Rossby number  $Ro = U/(fD)$  is also shown to control the eddy regime (Walker and Stewartson, 1972; Merkin and Solan, 1979; Boyer and Metz, 1983; Page, 1985), while the  $\beta$ -effect inhibits the process of separation (Merkin, 1980; Boyer and Davies, 1982). In a stratified, rotating fluid, the importance of stratification in the separation process can be quantified in terms of the Burger number  $Bu = (Ro/Fr)^2 = (R_d/D)^2$ , where  $R_d = NH/f$  is the baroclinic deformation radius (Davies et al., 1990b). For a vertically-sheared incoming flow, the overall baroclinic conversion process is sensitive to  $Bu$ . When  $Bu \geq 1$  (i.e.  $D \leq R_d$ ), the baroclinic conversion is negative and the eddy generation process is mainly due to barotropic conversion. When  $Bu < 1$  (i.e.  $D > R_d$ ) the baroclinic term changes sign and is positive. For smaller  $Bu$ , baroclinic instabilities are gradually favored and the overall baroclinic conversion process becomes larger and predominant (Dong et al., 2007).

The theoretical results on flow separation in presence of obstacles are successfully used in many cases to explain the dynamics around islands (Heywood et al., 1996; Tansley and Marshall, 2001; Coutis and Middleton, 2002). One can be tempted to extend these results in a straightforward fashion also to the case of capes. However, the dynamics of islands and capes can be significantly different for at least two main reasons: the presence of a lateral coast and the importance of sloping boundaries. Capes are not isolated features in the ocean as atolls or volcanic islands, but they are connected with the mainland. The presence of a coastline upstream and downstream the headland adds more lateral friction to the system and reduces the degrees of freedom of fluid motion. As a result, the critical Reynolds number needed to reach the eddy shedding regime is higher than for cylinders (Verron et al., 1991) and flow separation is somewhat inhibited. The Strouhal number decreases as a consequence and in different conditions drops to the typical value of  $St = 0.09$  (Boyer et al., 1987; Davies et al., 1990a). Moreover, capes are usually embedded in the shelf

and in its slope, allowing for different processes to occur. Firstly, the presence of a sloping obstacle introduces potential vorticity constraints, reducing barotropic instabilities and the tendency for eddy shedding (Klinger, 1993). Secondly, flow separation and eddy formation are influenced by the shelf topographic Rossby waves in a similar manner as the differential background rotation (Freeland, 1990). Thirdly, in case of stratified waters, the presence of a sloping obstacle allows the generation of lee waves (MacCready and Pawlak, 2001).

The study of cape dynamics relies on laboratory works (Boyer and Tao, 1987; Boyer et al., 1987; Davies et al., 1990a), field experiments (Geyer, 1993; Farmer et al., 2002; Pawlak et al., 2003; Edwards et al., 2004) and numerical results (Verron et al., 1991; Signell and Geyer, 1991; Davies et al., 1995; MacCready and Pawlak, 2001; Doglioli et al., 2004a).

The laboratory experiments of Boyer and Tao (1987) (hereinafter referred as BT87) address the case of *rotating stratified* flows impinging on a triangular prism cape with sloping sides. In the case of a right-side obstacle and for  $Bu < 0.2$ , the horizontal flow is fully-attached at all vertical levels. For somewhat larger Burger numbers,  $0.2 < Bu < 1$ , an attached anticyclonic eddy slowly forms in the lee of the obstacle. At still larger Burger numbers,  $Bu > 1$ , a well-defined eddy shedding regime is established. The aspect ratio  $\delta = H/D$  of laboratory experiments is generally very high compared to those in the real ocean. As a result, the obstacle used in BT87 corresponds to a very steep cape with slope  $\alpha = 1$ . As pointed out by the same authors, this geometry is far from being realistic. Even in coastal environments where capes can be very steep, the slope never reaches a value of  $\alpha = 1$ . Pawlak et al. (2003), for example, report a cape with slope  $\alpha = 0.2$ ; the promontory considered by Doglioli et al. (2004a), instead, has  $\alpha = 0.1$  while it is embedded in a much gentler sloping shelf. The coastal headland studied by Geyer (1993) has a much lower slope,  $\alpha = 0.015$  and larger scale features like the Gargano Promontory reach much lower values, like  $\alpha = 0.004$  (Cushman-Roisin et al., 2007; Veneziani et al., 2007). The variations in the slope directly reflect into the  $Re_f$  values underlining the increasing role of bottom friction for smaller aspect ratios. It remains not clear what is the role of topographic slope on the flow regimes behind a cape and if the observations made by BT87 are still valid for gentler slopes and more realistic scenarios.

Different observations underline that the interplay between sloping capes, rotation and stratification leads to complicated three-dimensional processes (Geyer, 1993; Farmer et al., 2002; Pawlak et al., 2003). Nevertheless, most of the numerical studies focus on the case of shallow water capes (Verron et al., 1991; Signell and Geyer, 1991; Davies et al., 1995), where the flow can be considered homogeneous and obeying vertically-integrated dynamics. Exceptions are the numerical works of Doglioli et al. (2004a) and MacCready and Pawlak

(2001) which are three-dimensional. However, the former considers a winter non-stratified quasi-homogeneous flow, while the latter neglects rotation. As a result, the effect of stratification in a rotating environment for a relatively deep cape has not been extensively explored thus far.

In this study, numerical simulations are carried out to pursue three main objectives. The first objective is to assess the sensitivity of the generation of turbulent coherent flow structures behind a cape to the combined effect of stratification and rotation. We keep the Rossby number constant at  $Ro = 0.06$ , and consider a geostrophically-balanced, steady barotropic current impinging on a headland under different stratified conditions. The second objective is to assess the effects of topographic slopes (or equivalently  $Re_f$ ) on the flow regimes. In order to cover the large slope range found in the literature and the ocean, we consider in our analysis five slopes:  $\alpha = 1$ ,  $\alpha = 0.1$ ,  $\alpha = 0.02$ ,  $\alpha = 0.01$  and  $\alpha = 0.005$  which corresponds to as many as  $Re_f$  values,  $Re_f = 208$ ,  $Re_f = 21$ ,  $Re_f = 4$ ,  $Re_f = 2$  and  $Re_f = 1$ . To our knowledge, this study represents the first three-dimensional numerical and systematical effort assessing the changes in the flow regimes at varying Burger and equivalent Reynolds numbers. The third objective is to quantify the implications of the different regimes in the force drag imparted from the cape to the coastal flow. In order to do that, we calculate the form drag coefficients for all the cases so far considered.

In agreement with the laboratory experiments of Boyer and Tao (1987), we find that the separation process is enhanced for increasing  $Bu$ . However, when gentler slopes (smaller  $Re_f$ ) similar to oceanic ones are considered, the importance of bottom friction increases and the same process is gradually more inhibited. Flow regimes diagrams in the  $Bu - \alpha$  space show that bottom friction is important especially near the bottom when  $Bu \geq 1$ . We also find that the form drag coefficient is at least 100 fold greater than the skin drag one and it reaches larger values for increasing Burger numbers and decreasing slopes (decreasing  $Re_f$ ). We empirically fit the values obtained from the runs to express with a function the dependency of the form drag coefficient on  $Bu$  and  $\alpha$ .

The paper is organized as follows. In section 2 the numerical model is presented together with a description of the numerical setups for all the simulations. The results are presented in section 3. In particular, sections 3.1 and 3.2 show the appearance of different flow regimes when the Burger number and the topographic slope are varied. Section 3.3 discusses the implication of these regimes on the different drags imparted on the coastal flow. A summary and concluding remarks are given in section 4.

CONSTANT PARAMETERS					
<i>Dimensional</i>			<i>Non-dimensional</i>		
$H$ [m]	$S_{bot}$	Temp. [°C]	$C_D$	$Ro$	$Re^*$
81	35	12.5	$3 \times 10^{-3}$	0.06	Implicit

Table 1  
Constant parameters for all the simulations.

## 2 Method

### 2.1 Numerical model

The numerical model used in this study is the Regional Ocean Modeling System (ROMS). ROMS solves the primitive equations and it is a hydrostatic terrain-following (sigma) coordinate model (Shchepetkin and McWilliams, 2005). Sigma coordinates are particularly useful in coastal applications because they resolve bottom boundary layer processes.

Since geophysical flows are characterized by large Reynolds numbers, in this study we decide to use ROMS ability to run with zero explicit numerical viscosity  $\nu^*$  and to just use the implicit viscosity built into the third-order, upstream-biased advection operator (Shchepetkin and McWilliams, 1998). The effective turbulent Reynolds number  $Re^* = UD/\nu^*$  is then established by the resolution of the grid: it represents the largest affordable  $Re^*$  with a certain discretization. The simulations are run with the ROMS default generic length scale algorithm (Umlauf and Burchard, 2003) which defines a  $k - \varepsilon$  turbulence closure with Canuto-A stability functions (Canuto et al., 2001). The skin bottom friction stress is calculated directly by the model according to the quadratic relation  $\vec{\tau}_b = -\rho_0 C_D \vec{v}_b \sqrt{u_b^2 + v_b^2}$ , where  $\vec{v}_b \equiv (u_b, v_b)$  is the bottom velocity and  $\rho_0$  the water density. The skin drag coefficient is always set to  $C_D = 3 \times 10^{-3}$  and therefore there is an one-to-one relation between the slope and  $Re_f$ . No-slip boundary conditions are simulated by the model via a specific land-masking rule (see discussion in Dong et al., 2007) even when  $\nu^* = 0$  (Shchepetkin and O'Brien, 1996).

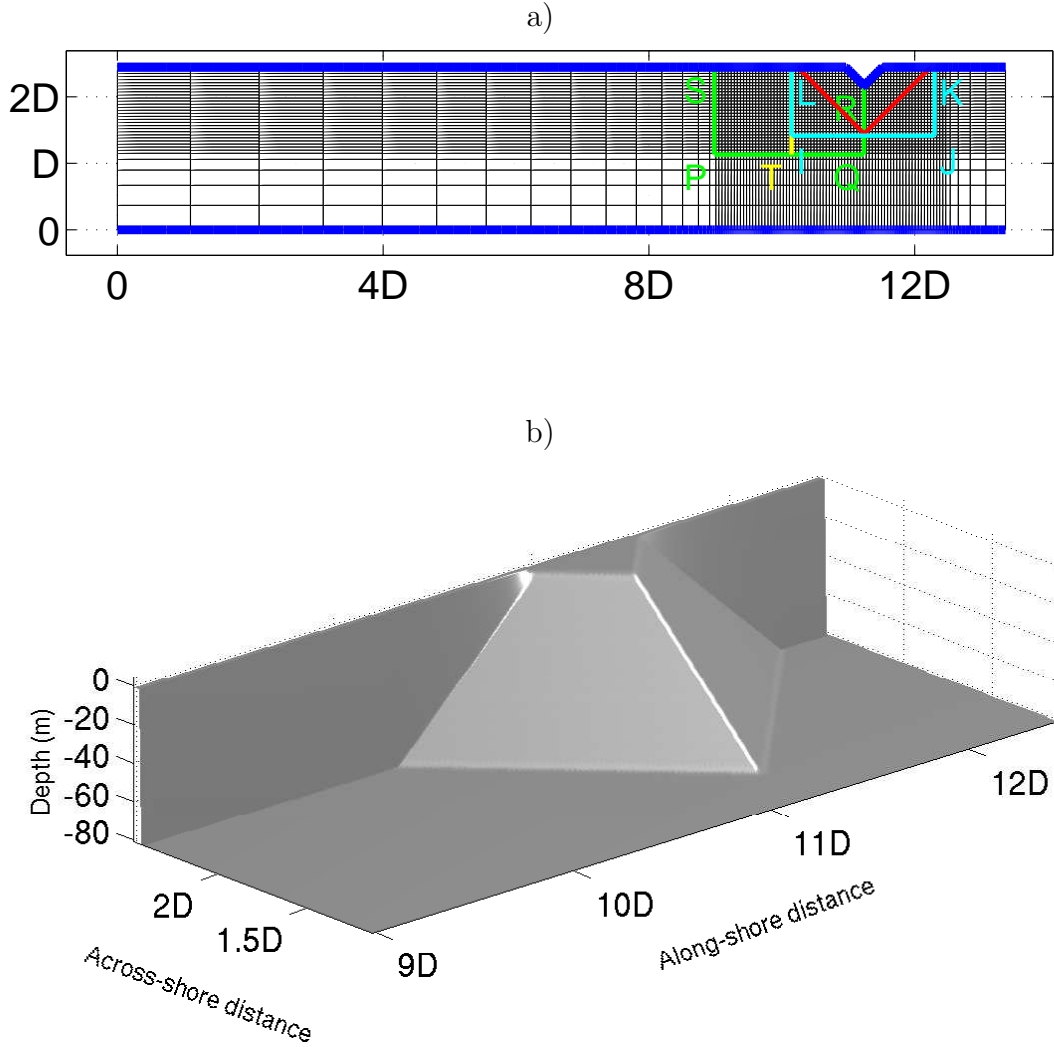


Fig. 1. Numerical setup expressed in terms of  $D$ .  $D$  is defined as the across-shore horizontal dimension of the obstacle at the bottom. a) Plan view of the horizontal grid. For clarity, every third grid-point is shown in the picture. The northern and southern boundaries are closed (blue thick line) while the eastern and western are open. The red line indicates where the slope terminates. The areas P (yellow), IJKL (cyan) and PQRS (green) are functional to later calculations of the vertical velocity, the kinetic energy and the form drag, respectively. b) Three-dimensional shape of the cape.

## 2.2 Numerical setup

Coastal capes have characteristic horizontal dimensions which can scale from  $D \sim 1$  km to  $D \sim 100$  km. In the case of shallow waters ( $H \sim 10$  m), the dynamics around headlands are known to be dominated by bottom frictional



		<i>Bu</i>								
		0.0	0.05	0.10	0.30	0.50	0.70	1.00	3.00	6.48
<i>Re<sub>f</sub></i> ( $\alpha$ )	208 (1)	x	x	x	x	x	x	x	x	x
	21 (0.1)		x					x		x
	4 (0.02)		x					x		x
	2 (0.01)		x	x	x	x		x		x
	1 (0.005)		x			x		x		

Table 2  
The matrix of the numerical simulations for this study.

effects (Signell and Geyer, 1991; Davies et al., 1995). For relatively deep waters ( $H \sim 100$  m) the dynamics are less clear and more interesting. Complicated three-dimensional phenomena are shown to take place and to be strongly dependent on the system parameters (Geyer, 1993; Farmer et al., 2002; Pawlak et al., 2003; Doglioli et al., 2004a). In these cases, if typical values of  $C_D \sim 10^{-3}$ ,  $f \sim 10^{-4} \text{ sec}^{-1}$ ,  $U \sim 0.1 \text{ m sec}^{-1}$  and  $N \sim 3 \times 10^{-3} \text{ sec}^{-1}$  are considered, it is possible to calculate realistic ranges for the parameters  $Ro$ ,  $Bu$  and  $Re_f$ , namely:  $10^{-2} < Ro < 1$ ;  $10^{-3} < Bu < 10$ ; and  $1 < Re_f < 100$ .

In all the simulations the obstacle is a triangular prism with sloping boundaries lying on a flat bottom (see Fig. 1b) and the domain of integration is a zonal channel discretized with a rectangular unevenly spaced grid of  $285 \times 100$  points (Fig. 1a). The mesh size increases in both the along and across directions moving away from the obstacle. The most resolved interior area around the cape has a horizontal resolution of  $\Delta = D/65$  in all the simulations, while the vertical resolution relies on 20 sigma layers. Open boundaries are located at the east and at the west of the domain while a no-slip condition on a rigid wall is implemented at the north and at the south (see Fig. 1a). The simulations are forced by inflow conditions at the open boundaries. Here the Flather condition is used for the averaged velocities, while radiation conditions are used for the sea surface height, baroclinic velocities and the tracers. At the boundaries the tracers are relaxed toward the initial values in an area of six grid points to facilitate the radiation outside the numerical domain. The stratification is induced by a linear increase in the initial salt distribution with depth, while the temperature is held constant.

In all simulations, the characteristic vertical dimension is set to  $H = 81$  m, the constant temperature to  $12.5^\circ\text{C}$  and the bottom salinity to  $S_{bot} = 35$  (the surface value  $S_{surf}$  is varied at varying stratification). The Rossby number  $Ro$

is also held fixed at the realistic value of  $Ro = 0.06$ , that is very close to the one used in the photographed experiments of BT87 thus allowing for a convenient visual comparison between our results and the ones observed in the laboratory. The parameters held always constant are listed in Table 1.

The main non-dimensional parameters varied in this study are the Burger number  $Bu$  and the equivalent Reynolds number  $Re_f$ . This latter is changed by varying the slope of the obstacle  $\alpha$ . We span the ranges  $0 \leq Bu \leq 6.48$  and  $1 \leq Re_f \leq 208$  ( or  $0.005 \leq \alpha \leq 1$ , see Table 2). The horizontal dimension  $D$ , the rate of rotation  $f$ , the surface salinity value  $S_{srf}$  and the inflow unperturbed velocity  $U$  are varied according to the values of  $Bu$  and  $\alpha$ , with the additional constraint of constant  $Ro$ . The whole set of dimensional and non-dimensional values for the performed experiments are listed in Table 3. The first block of nine experiments cover the range of the BT87 laboratory experiments, characterized by  $\alpha = 1$  and increasing  $Bu$ . The other experiments investigate the dynamics at gentler (and more realistic) slopes.

The external value for the normal velocity to the open boundaries is prescribed according to the Rossby number  $U_b = Ro f D$ , while the value for the sea elevation is needed to sustain geostrophically with its gradient such a velocity. The value for the tangential velocity is set to  $V_b = 0$  m/s. To simulate a sudden start comparable with the BT87 experiment, all the simulations begin with  $U = U_b$  prescribed in the whole domain.

The simulations run until  $\tau = 25.92$ , where  $\tau$  is the dimensionless advective time defined as  $\tau = tU/D$ . Time-steps are varied always respecting the CFL condition. For example, the nine simulations for the first set of experiments are run with baroclinic and barotropic timesteps of  $\Delta t_i = 0.5$  sec and  $\Delta t_e = 0.025$  sec, respectively. In order to achieve  $\tau = 25.92$ , the model cycles in this case for 86400 time iterations and each simulation requires a wall-clock time of four days using a single processor.

For the same typical values, the  $\beta$ -effect is expected not to play a significant role, since  $10^{-4} < \beta D/f < 10^{-2}$ . In contrast, topographic Rossby effects can be relevant, given the steep slope of some cases. However, this study is limited to the case where the obstacle lies on the right hand side of the in-coming current and we expect topographic waves not to alter the flow significantly because they propagate in the same direction as the main current (Freeland, 1990).

VARIABLE PARAMETERS						
	<i>Dimensional</i>				<i>Non-dimensional</i>	
Exp.	$D$ [km]	$U$ [m sec <sup>-1</sup> ]	$f$ [sec <sup>-1</sup> ]	$S_{srf}$	$Re_f$ ( $\alpha$ )	$Bu$
1	0.13	0.078	$10^{-2}$	35.00	208 (1)	0.00
2	0.13	0.078	$10^{-2}$	34.86	208 (1)	0.05
3	0.13	0.078	$10^{-2}$	34.74	208 (1)	0.10
4	0.13	0.078	$10^{-2}$	34.18	208 (1)	0.30
5	0.13	0.078	$10^{-2}$	33.64	208 (1)	0.50
6	0.13	0.078	$10^{-2}$	33.08	208 (1)	0.70
7	0.13	0.078	$10^{-2}$	32.27	208 (1)	1.00
8	0.13	0.078	$10^{-2}$	26.76	208 (1)	3.00
9	0.13	0.078	$10^{-2}$	17.61	208 (1)	6.48
10	1.30	0.078	$10^{-3}$	34.86	21 (0.1)	0.05
11	1.30	0.078	$10^{-3}$	32.27	21 (0.1)	1.00
12	1.30	0.078	$10^{-3}$	17.61	21 (0.1)	6.48
13	6.50	0.039	$10^{-4}$	34.96	4 (0.02)	0.05
14	6.50	0.039	$10^{-4}$	34.32	4 (0.02)	1.00
15	6.50	0.039	$10^{-4}$	30.52	4 (0.02)	6.48
16	13.0	0.078	$10^{-4}$	34.86	2 (0.01)	0.05
17	13.0	0.078	$10^{-4}$	34.74	2 (0.01)	0.10
18	13.0	0.078	$10^{-4}$	34.18	2 (0.01)	0.30
19	13.0	0.078	$10^{-4}$	33.64	2 (0.01)	0.50
20	13.0	0.078	$10^{-4}$	32.27	2 (0.01)	1.00
21	13.0	0.078	$10^{-4}$	17.61	2 (0.01)	6.48
22	26.0	0.156	$10^{-4}$	34.45	1 (0.005)	0.05
23	26.0	0.156	$10^{-4}$	29.52	1 (0.005)	0.50
24	26.0	0.156	$10^{-4}$	24.00	1 (0.005)	1.00

Table 3  
Varying parameters for all the simulations.

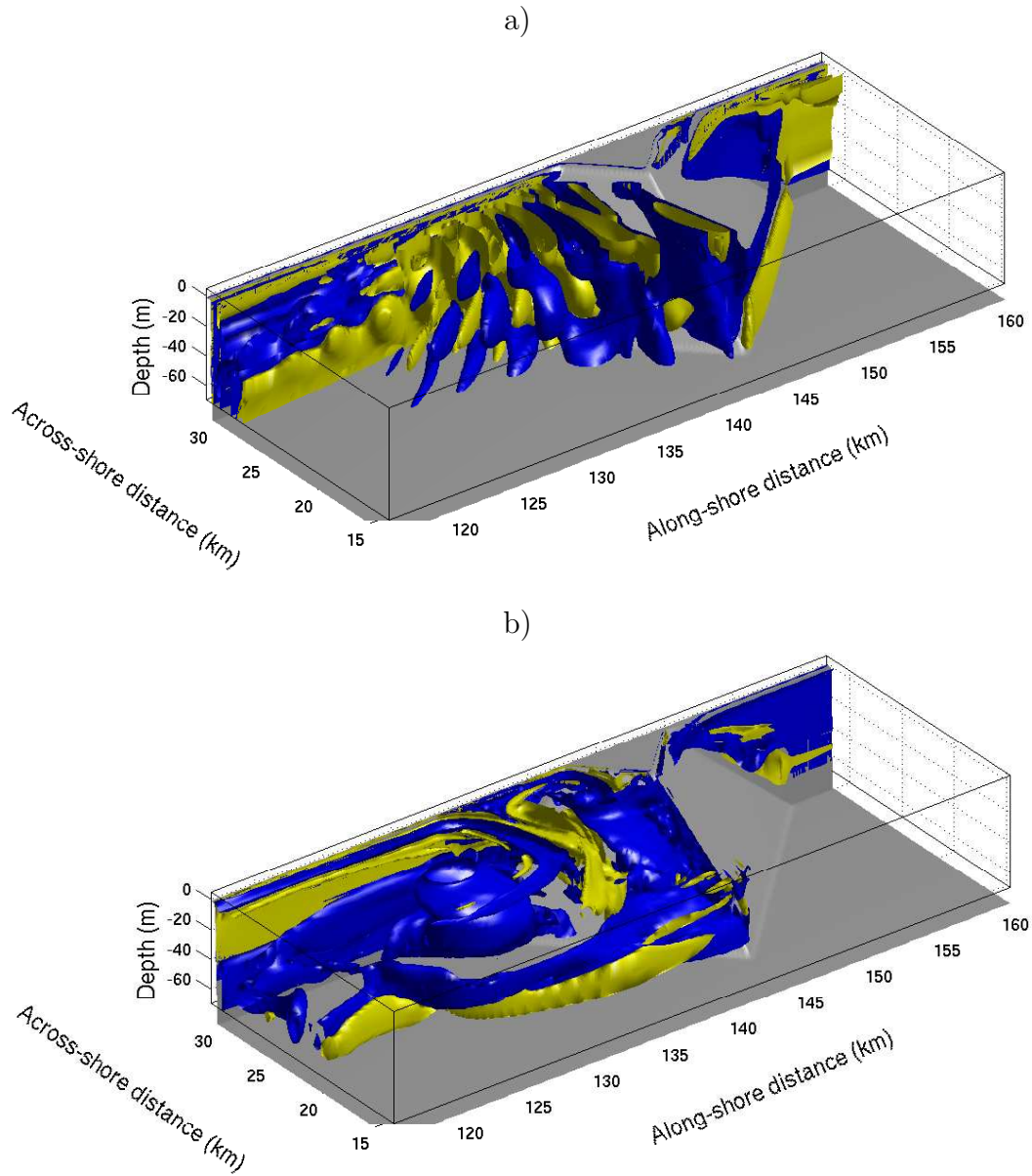


Fig. 2. Three-dimensional views of relative vorticity iso-surfaces in the vicinity of the cape. Negative values are shown in blue, while positive values are in yellow. a) Exp. 16: a typical example of fully-attached regime, when no separation occurs and lee waves are evident in the lee of the obstacle. b) Exp. 21: an example of eddy shedding regime. The flow is almost two-dimensional and flow separation is observed behind the cape.

### 3 Results

Different flow regimes can be observed in the numerical experiments listed in Table 3. Fig. 2 provides a visual idea of flow regimes at constant slope ( $\alpha = 0.01$ ) but at different Burger numbers. It also underlines the complexity and the three-dimensional structure of the different turbulent features appearing behind the cape. Fig. 2a shows vorticity surfaces for the fully-attached regime when  $Bu = 0.05$ . In this case the horizontal flow follows the obstacle at different vertical levels and no separation behind the obstacle is observed. Vertical movements are due to the presence of lee waves evident as elongated oscillating structures behind the obstacle. Fig. 2b shows an eddy shedding regime when  $Bu = 6.48$ . Vertical movements are restricted and the flow is more two-dimensional. As a result, a separation area is observed behind the obstacle and coherent eddies form behind the cape.

To put order in describing the totality of the regimes, it is convenient to initially restrict our attention to simulations having the same parameters of the BT87 laboratory experiments. We then consider gentler slope cases as the ones that can be found in the ocean.

#### 3.1 Flow regimes for $\alpha = 1$ ( $Re_f = 208$ )

We first analyze the case with  $\alpha = 1$  to compare the flow regimes obtained running ROMS with the BT87 laboratory experiment. It is useful to recall the main findings of the BT87 work. For a right side obstacle, BT87 show the appearance of three different regimes corresponding to a gradual increase of stratification: (i) a fully-attached regime for low Burger numbers ( $Bu < 0.2$ ), (ii) an eddy-attached regime for intermediate Burger numbers ( $0.2 < Bu < 1$ ) and (iii) an eddy shedding regime for high Burger numbers ( $Bu > 1$ ).

Figures 3 and 4 show vorticity and velocity snapshots obtained when the numerical model is integrated. The fields are shown at three different depths and for increasing  $Bu$ . In the homogeneous case ( $Bu = 0.00$ , Fig. 3a, b and c), potential vorticity conservation constrains the generation of small anticyclones in the stripe over slope topography. However, since the geometry of the obstacle is symmetric, an upstream decrease in relative vorticity due to the presence of shallower waters corresponds with an equal downstream increase as the waters become deeper. As a result, all the vorticity gradients are confined above the slope and nothing significant can be observed downstream the obstacle at any depth.

The presence of stratification, even if very weak, changes the dynamics. For small Burger numbers,  $Bu = 0.05$ , no eddies are present. The flow tends to

$$\alpha = 1 (Re_f = 208)$$

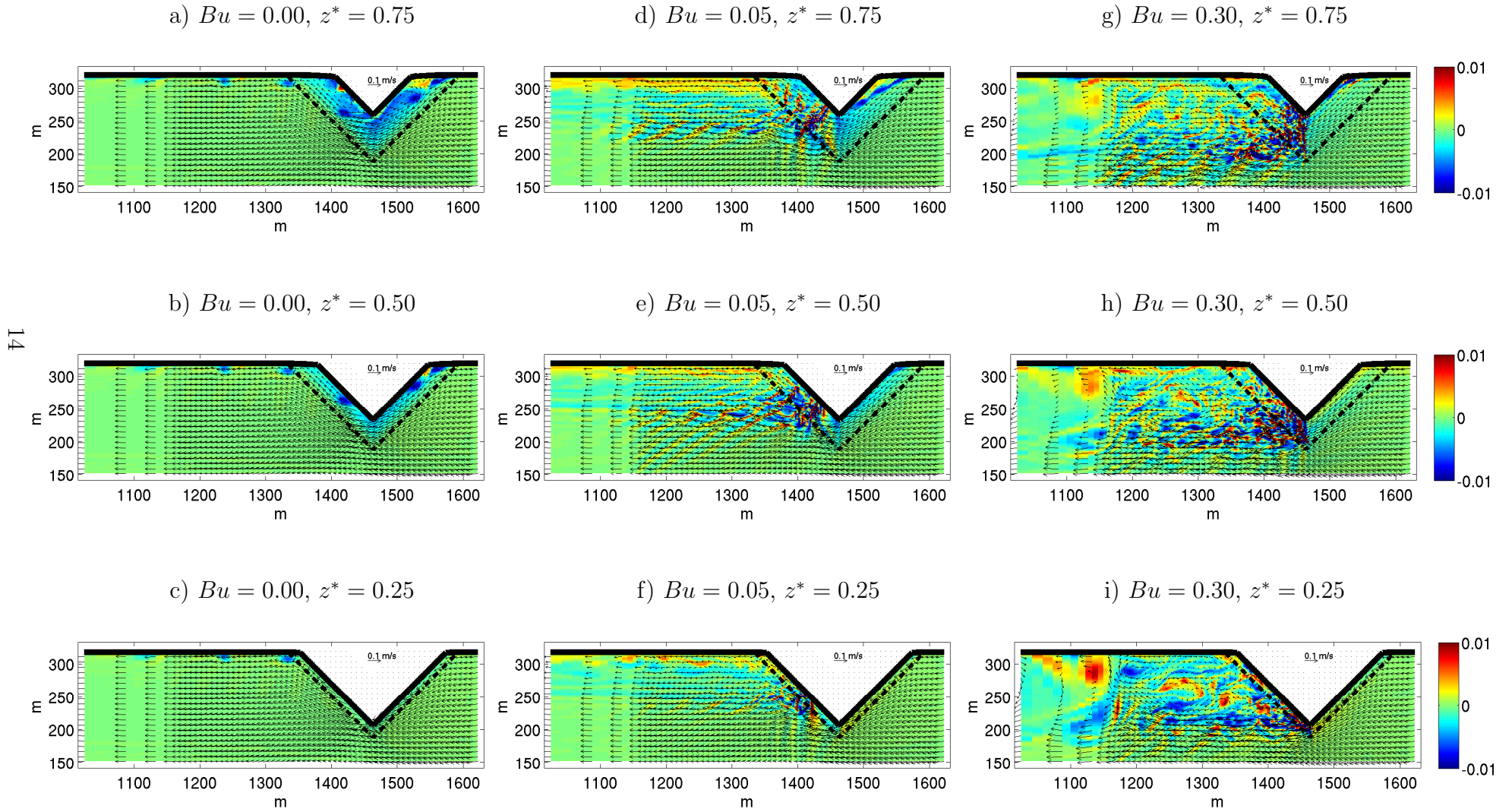


Fig. 3. Close up of relative vorticity [ $\text{sec}^{-1}$ ] and velocity vectors at three different levels of the water column ( $z^* = z/H$ ) after  $\tau = 9.936$  for the  $\alpha = 1$  simulations. The black dash-dotted line indicates where the slope terminates.

$$\alpha = 1 (Re_f = 208)$$

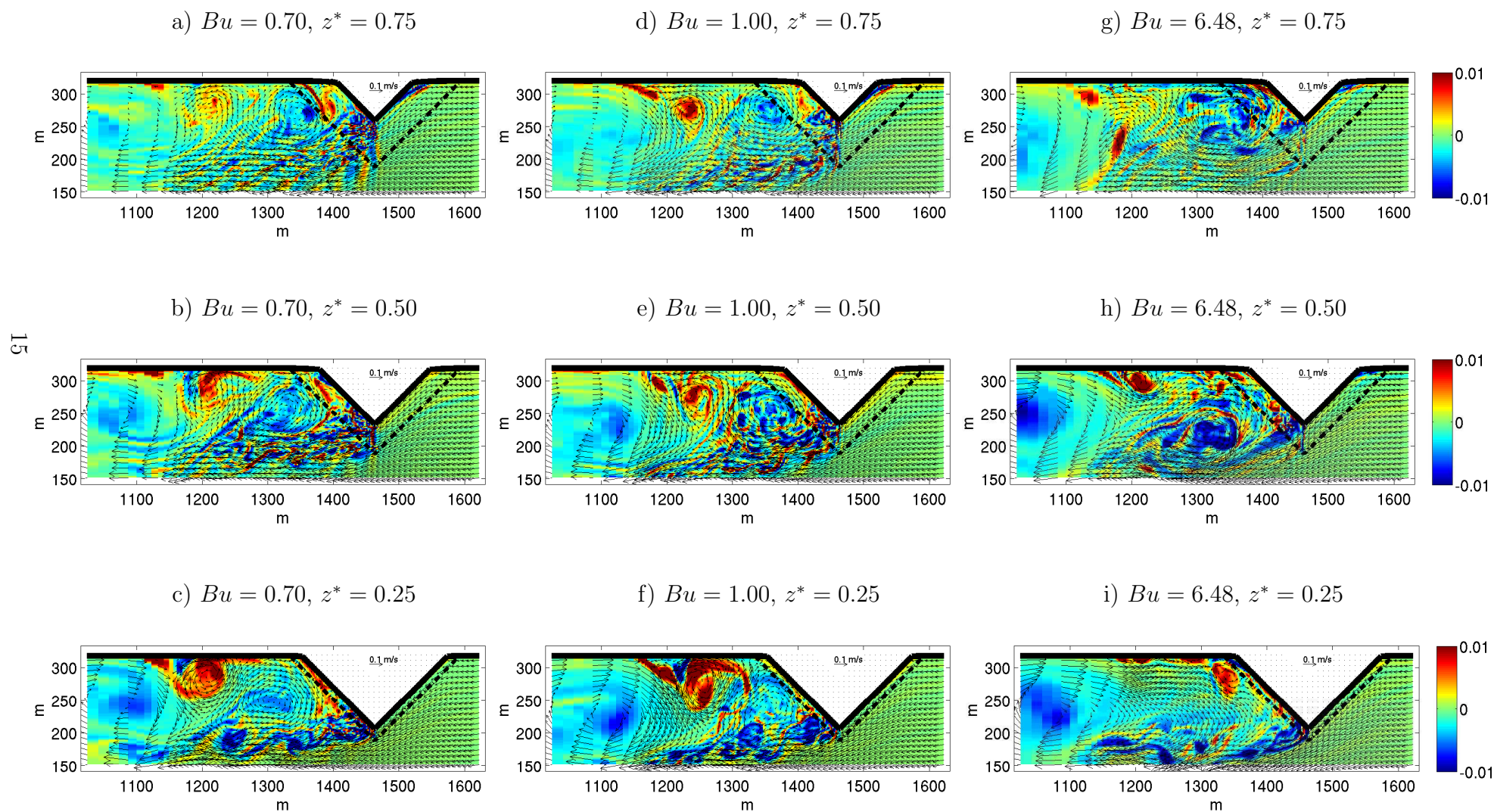


Fig. 4. As in Fig. 3 but for different  $Bu$ .

follow the obstacle at all levels (fully-attached regime, Fig. 3d, e and f). At the same time, a clear oscillating signal in the vorticity field can be observed starting from the tip of the cape and continuing downstream. The signal is associated with the formation of lee waves as the flow goes over the ridge of the cape. If we increase further the Burger number,  $0.10 \leq Bu \leq 0.30$ , small-scale eddies form at surface in the lee of the cape and they drift downstream away from the obstacle as isolated small features (Fig. 3g). The strongest of these smaller eddies come from the area close to the tip of the cape. We therefore refer to this turbulent regime as tip-eddy regime. At depth some of these tip eddies merge to form larger scale structures (Fig. 3h and i). For higher Burger numbers,  $0.50 \leq Bu \leq 0.70$ , the same structures gradually grow and occupy all the space available in the lee of the cape. Their diameter is comparable at every depth with the across-shore obstacle dimension at that level. We refer to these larger eddies as lee eddies. Due to the direction of the incoming current, the first eddy forming in the lee is an anticyclone. Its interaction with the sides of the obstacle causes the formation of a lee cyclone. This latter also grows in time and, with its growth, it allows the detachment of the first eddy from the wall. At the same time a second lee anticyclone can start forming. When the second lee anticyclone occupies the whole lee of the cape, the cyclone is also pushed downstream and it sheds from the cape. The cyclone interacts with the first anticyclone forming an eddy pair which advects downstream. Once the pair sheds from the cape, a second one forms in the lee and the cycle is repeated. For these  $Bu$  values, an eddy shedding regime is therefore established. Initially the lee eddies are weak and they do not appear as coherent vorticity features even if their strength increases with depth (Fig. 4a, b and c). A weaker signal of the presence of lee waves can still be observed at surface, while at the bottom, smaller tip eddies still form close to the apex of the obstacle and they are advected along the periphery of the larger lee anticyclone. For  $Bu = 1.00$ , the eddy shedding regime is more evident because the eddies are stronger and more coherent than before at all depths (Fig. 4d, e and f). Finally, for large stratification,  $Bu = 6.48$ , the eddies are more elongated and stronger (4g, h and i).

In our simulations, two of the regimes observed in the laboratory are evident. For  $Bu < 0.1$  the fully-attached regime appears behind the obstacle as well as the eddy shedding for  $Bu \geq 1$  values. For intermediate  $Bu$ , however, the numerical model makes a rapid transition from the fully-attached regime to tip eddies which gradually organize and shed more for increasing stratifications. Irrespective of the value for  $Bu$ , the BT87 eddy-attached case is not reproduced in our runs and seems to describe only a transitional state between the fully-attached and the eddy shedding regimes. We speculate that its relative importance in the laboratory experiments should be attributed to important features which cannot be reproduced in our simulations. For example, the BT87 experimental apparatus has a rigid Plexiglas lid on the top of the tank. This lid can introduce additional friction and the same authors



$$\alpha = 1$$

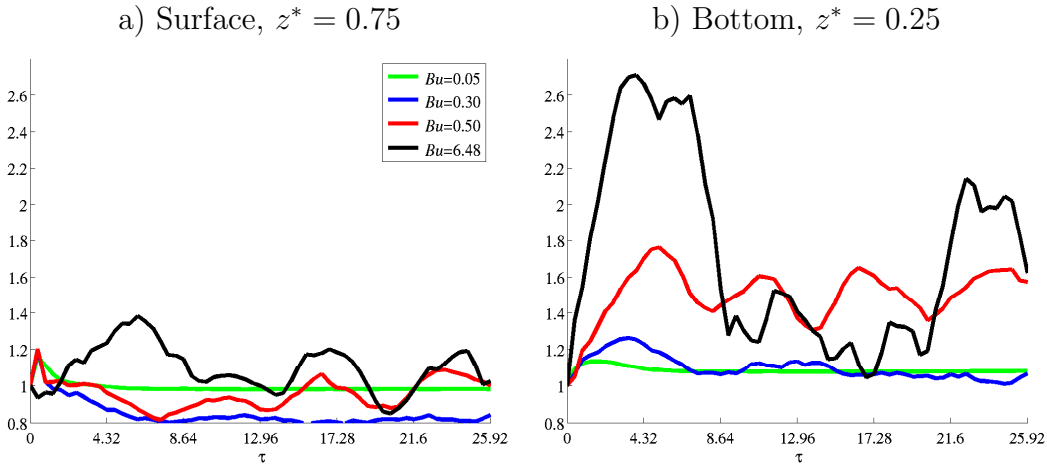


Fig. 5. The ratio  $KE/KE_0$  in time for varying Burger numbers  $Bu$ . The obstacle slope is  $\alpha = 1$  in all the considered simulations.

observe spin down effects on the weaker turbulent structures at the surface of the tank. Moreover, at the high aspect ratio of the BT87 case, the hydrostatic approximation can be questionable even if, for small Rossby numbers, the dynamics should remain hydrostatic. Pedlosky (1987) shows that the hydrostatic limit occurs when  $l_{hydr} = \min(\delta^2, \delta^2 Ro) \ll 1$ , and in this study  $1.5 \times 10^{-6} < l_{hydr} < 6 \times 10^{-2}$ . Nevertheless we believe that the eddy-attached case is not reproduced mainly because of the difference between Reynolds numbers used in laboratory experiments versus numerical simulations. BT87 deal with a real fluid, characterized by its viscosity and Reynolds number  $Re$ . Ocean models, instead, have to rely on numerical viscosity  $\nu^*$  to remove and avoid accumulation of energy at smaller scales and our simulations are run at the largest  $Re^*$  affordable with our resolution. The enhanced role of viscosity in the laboratory can explain the importance of the eddy-attached case respect to the numerical results.

The normalized kinetic energy budget per unit mass,  $KE/KE_0$ , calculated over the area PQRS of Fig. 1, is used to follow the temporal evolution of the flow. Here  $KE_0 = KE(z, t = 0)$ .  $KE/KE_0$  is shown at the surface and near the bottom for varying  $Bu$  in Fig. 5. When  $Bu = 0.05$ , where no separation occurs,  $KE/KE_0$  remains flat and steady at all levels and times. When  $Bu = 0.30$ , an oscillating signal appears. This is consistent with the emergence of the tip eddies regime observed before. When  $Bu = 0.50$ , the lee eddy shedding regime is evident in the kinetic energy pattern. We can easily count four distinct maxima. The shedding regimes appear to be in phase at different levels

and stronger with increasing depths. For increasing  $Bu$ , the shedding regimes are always in phase and gradually more energetic. However, the number of peaks associated with the shedding decreases.

Summarizing, in the  $\alpha = 1$  case, we can observe a clear general trend for varying Burger numbers. For low  $Bu$  we observe a fully-attached regime while, increasing the Burger number, eddy generation is gradually more evident until a clear shedding regime is established for higher  $Bu$ . These results match well the idea that the eddy shedding regime is enhanced if the flow remains more horizontal than vertical. If stratification is increased, vertical movements are also reduced and fluid particles are forced to go more around the obstacle than over it. As a result their trajectories are more and more two-dimensional and the separation process is more probable to appear than lee wave generation.

### 3.2 Flow regimes for $\alpha < 1$ ( $Re_f < 208$ )

We now describe the results when different obstacle slopes are considered for varying Burger numbers. With respect to the previous  $\alpha = 1$  case, bottom friction is expected to be more influential for gentler slope simulations. In analyzing our results, we have to take into account contrasting effects. On one hand, bottom friction is expected to gradually damp turbulent structures with gentler slopes, inhibiting lee eddy formation. On the other hand, high stratification values are expected to gradually favor separation and eddy generation in the surface layers for two different reasons. Firstly, strong stratification reduces vertical movements forcing particle trajectories to be more and more two-dimensional. Secondly, a strong stratification shields surface layers from bottom friction confining its inhibiting effect more to the deeper layers. These effects can be clearly seen in the  $\alpha = 0.01$  cases (Fig. 6). For  $Bu = 0.05$ , the regime is again fully-attached even if the lee wave signal is less noisy. Its intensity decreases with depth and lee waves almost disappear in the layer closer to the bottom (Fig. 6a, b and c). When  $Bu = 1.00$ , bottom friction influences most of the water column since stratification is still not so important to shield the top layers. Near the surface an eddy shedding can still be observed and the sequence of eddy pairs is very regular and periodic (Fig. 6d). In the middle of the water column, the evident eddy shedding regime of the steeper case is generally inhibited. Moreover, after the formation of the first lee anticyclone, different tip eddies move along its periphery while the lee eddy does not shed and stays attached to the cape. The occasional presence of small cyclones allows the shedding of small features from the tail of the lee anticyclone. As a result, the detachment of the eddies from the cape does not happen at the lee but further downstream (Fig. 6e). At the bottom, the anticyclone rapidly decays due to bottom friction and the eddy shedding is just due to tip eddies traveling around its periphery (Fig. 6f). For  $Bu = 6.48$ , the increasing stratifi-



cation limits frictional effects to near bottom layers. At the surface and in the middle of the water column, stronger and wider lee eddies form downstream the cape. They become more elongated to finally detach much later from the obstacle than for  $Bu = 1.00$  (Fig. 6g and h). At the bottom, the initial strong lee anticyclone spins down and the tip eddy shedding almost completely disappears. What is left is a big separation area which remains attached to the cape for the rest of the simulation (Fig. 6i). We refer to this situation as an eddy-attached regime.

Summarizing in the  $\alpha < 1$  case, namely for slopes similar to the oceanic ones, bottom frictional effects are more important than in the laboratory experiments. For gentler slope cases, lee eddies are larger and bottom friction can act on the wider bottom eddy surface. As a result, bottom friction damps and spins down turbulent structures and bottom flow regimes can differ from surface ones.

As before, we can visualize the time trends of the flow regimes with the help of the ratio  $KE/KE_0$ . In order to assess just the role of the obstacle slope, here we just choose to show the simulations with  $Bu = 1.00$  and where just  $\alpha$  is varied. Fig. 7 shows the values for  $KE/KE_0$  at the surface and at the bottom. When  $\alpha = 1$ , an eddy shedding regime is present. The maxima due to the shedding are three and in phase at different depths. They are more energetic if we move toward the bottom layers. For  $\alpha = 0.1$ , the effect of bottom friction starts to be felt. At all depths the shedding is less energetic than before. However the frequency of the peaks slightly increases even if the layers are still in phase with each other. A drastic difference is observed for gentler slopes. For  $\alpha = 0.05$ , the shedding regime is so reduced that the flow can be considered eddy-attached while, at the surface, three distinct peaks can still be found. For gentler slopes,  $\alpha = 0.01$  and  $\alpha = 0.005$ , these trends are gradually more evident. At the bottom the first lee eddy does not form and just tip eddies can be observed. At surface, the lee eddy shedding still persists and the shedding frequency gradually increases for gentler slopes. We can count four maxima for  $\alpha = 0.01$  and five when  $\alpha = 0.005$ .

Since  $KE/KE_0$  accurately reflects the flow characteristics shown in the snapshots, we can use the time evolution of this quantity to tell apart the different flow regimes in the simulations. The concept behind this idea is the following. In the case of a fully-attached regime, the  $KE/KE_0$  trend is completely flat and steady in time and this is reflected in a very low standard deviation. The emergence of tip eddies increases the time variability of the trend and the standard deviation is expected to slightly increase. When a lee eddy shedding regime appears, the variability increases more while, for a more energetic lee eddy shedding regime, it is expected to result even larger. The only flow regimes escaping this simple criterion are the ones strongly influenced by bottom friction. In this cases, the effect of the bottom is so important as to spin

$$Bu = 1.00$$

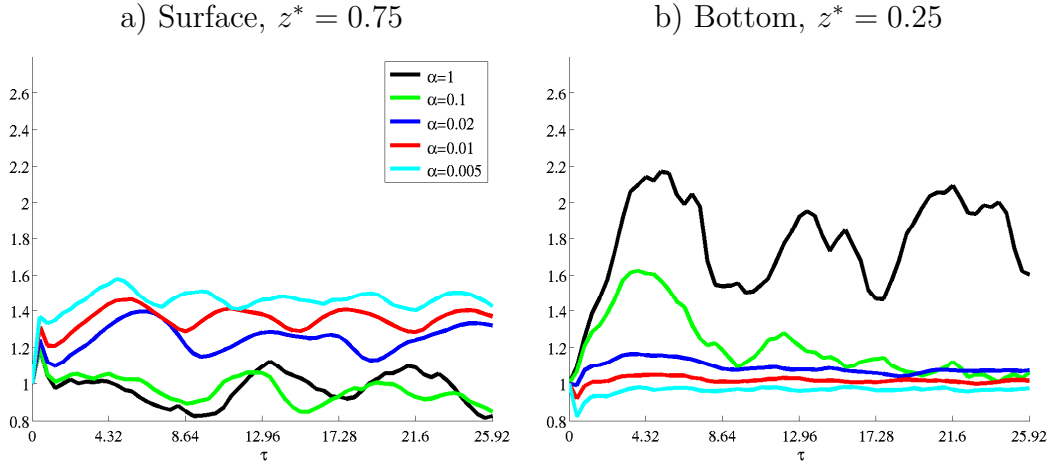


Fig. 7. The ratio  $KE/KE_0$  in time for varying obstacle slopes  $\alpha$ . The Burger number is  $Bu = 1.00$  in all the considered simulations.

down the first lee eddies. If the eddy shedding is initially very energetic, bottom friction gradually weakens the flow and the intensity of the eddies shed. Otherwise, bottom friction spins down the first lee anticyclone so much to establish an eddy-attached regime. Both these cases, however, are easily recognizable since  $KE/KE_0$  neither stays flat nor oscillates. Rather, it decays in time indicating a gradually weakening of the flow. Details of this classification are reported in the appendix.

Once this classification is performed, a flow regime diagram in the  $Bu - \alpha$  space can be drawn. Figures 8a and 8b show this diagram for the surface and the bottom layer, respectively. Figure 8a underlines how surface regime are strongly dependent on  $Bu$  and almost independent of  $\alpha$ . For low  $Bu$ , the fully-attached regime extends for all the slope values considered in this study. For high aspect ratios and increasing  $Bu$ , tip eddies are followed by a lee eddy shedding regime. For high  $Bu$  this regime becomes stronger and more evident. When we decrease the slopes, a general inhibition due to bottom friction effects can be observed. The eddy shedding regime is gradually reached at higher  $Bu$  and, for most of the intermediate Burger numbers, it is replaced by tip eddies. This shift in the regime happens more gradually for gentler slopes.

The situation changes for the layer close to the bottom since for  $Bu \geq 1$  the dynamics are controlled by  $\alpha$ . When  $\alpha = 1$ , the scenarios are similar to the surface. This is expected since the bottom friction does not play such a role for high aspect ratios. For gentler slope cases, lee eddies are larger and their surface in contact with the sea-floor is proportionally wider. Bottom friction

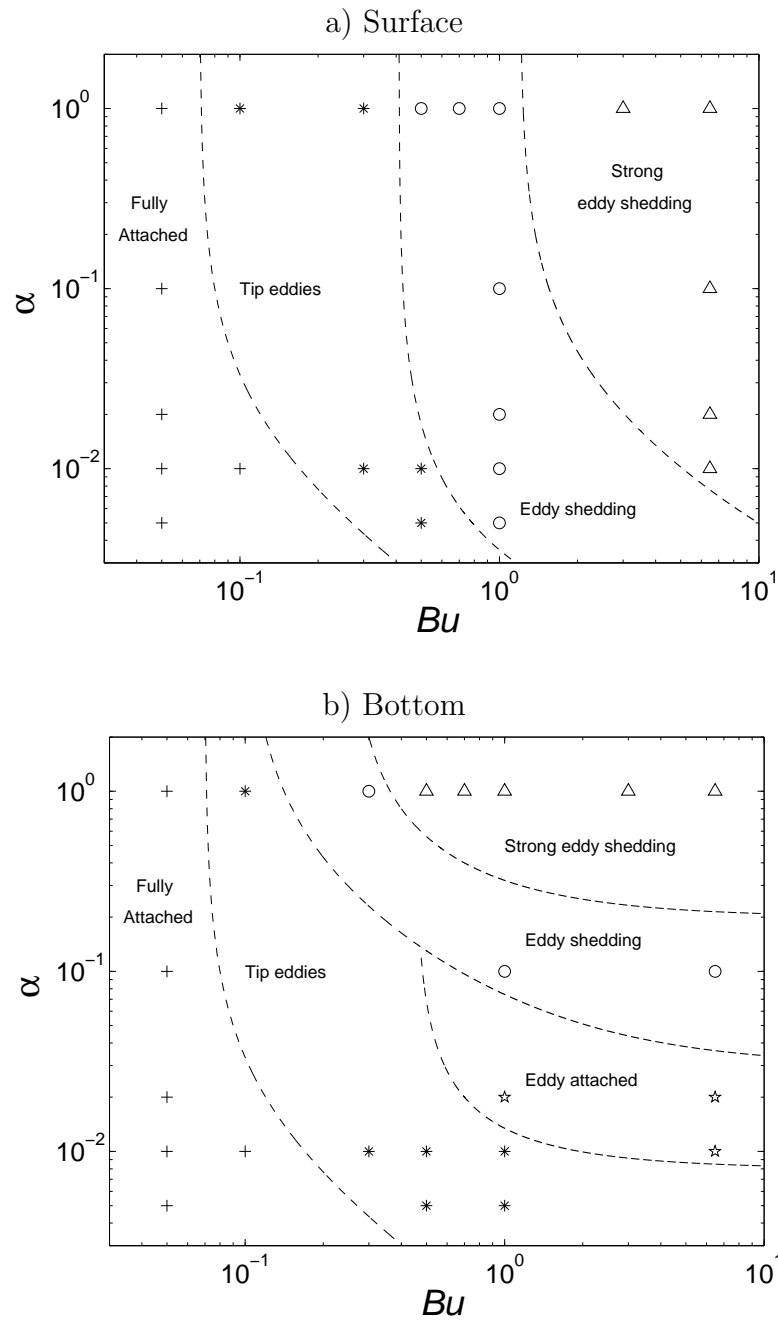


Fig. 8. Different regimes varying  $Bu$  and the slope  $\alpha$  for a) surface and b) bottom. Note that both axes are logarithmic. The regimes are: fully-attached (+), tip eddies (\*), eddy-attached ( $\star$ ), eddy shedding (o) and strong eddy shedding ( $\Delta$ ). The dashed lines are the approximate divisions between the regimes.

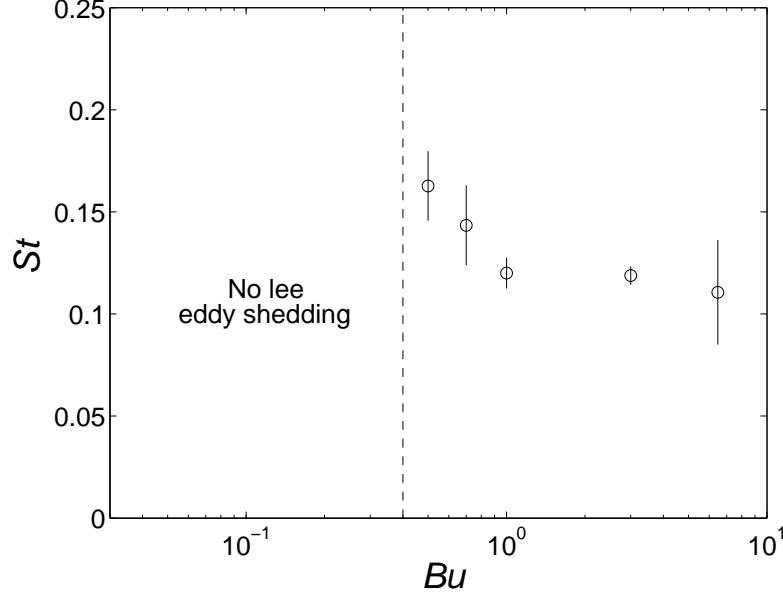


Fig. 9. Strouhal number as a function of  $Bu$  for  $\alpha = 1$ . Error bars indicate standard deviations.

can decelerate the flow and spin down the first lee eddy forming. As a result, the strong eddy shedding gradually disappears and eventually leaves space to the eddy-attached regime. When the importance of bottom friction increases more, a lee eddy cannot even form and we are left just with small tip eddies.

The time evolution of  $KE/KE_0$  of Fig. 5 and 7 already shows important differences in the lee shedding frequency. In order to quantify these differences, the Strouhal number is calculated. The period of the shedding is measured by the time taken for the centers of successive anticyclones to pass the across-shore section  $\overline{PQ}$  shown in Fig. 1a. Fig. 9 indicates that  $St$  decreases for increasing Burger numbers and for high  $Bu$  gets close to the value 0.09 registered in other works under different conditions (Boyer et al., 1987; Davies et al., 1990a).

In order to show that vertical movements are reduced with increasing  $Bu$  numbers, we calculate the quantity

$$w^* = \frac{1}{U\delta(\tau_2 - \tau_1)A_{PTLS}} \int_{\tau_1}^{\tau_2} \int_{A_{PTLS}} c_f w^{rms} dA,$$

where  $\tau_1 = 4.32$ ,  $\tau_2 = 25.92$ ,  $A_{PTLS}$  is the projected area shown in Fig. 1, and

$$w^{rms}(x, y, t) = \sqrt{\frac{1}{\eta(x, y, t) - b(x, y)} \int_b^\eta w^2(x, y, z, t) dz},$$

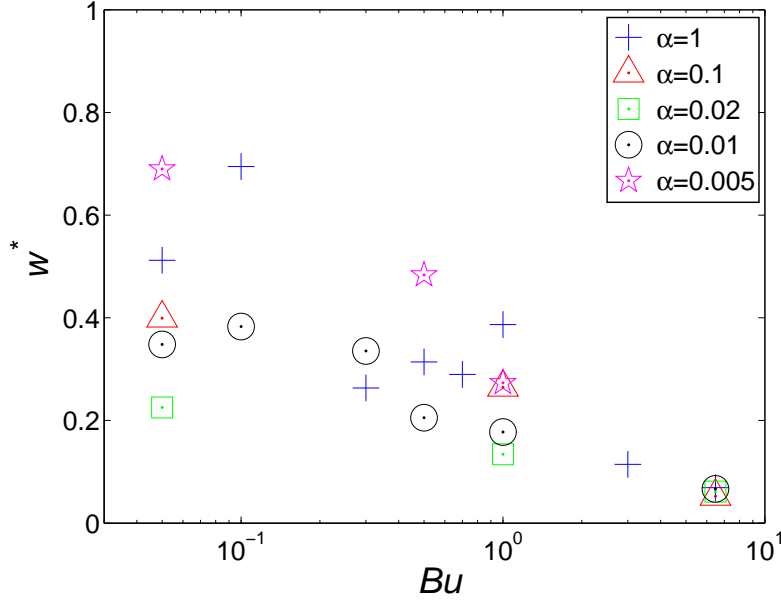


Fig. 10. The quantity  $w^*$  as a function of  $Bu$  and  $\alpha$ . Note that the  $x$ -axis is logarithmic.

$$c_f(x, y, t) = \begin{cases} 1 & \text{if } w^{rms} > 0.2 \times \max(w^{rms}), \\ 0 & \text{if } w^{rms} \leq 0.2 \times \max(w^{rms}). \end{cases}$$

In Fig. 10  $w^*$  is plotted in function of  $Bu$  for all the experiments. The general trend is a reduction of  $w^*$  for increasing  $Bu$ . However, if vertical movements are clearly suppressed for  $Bu \geq 1$ , a larger scattering can be observed for lower Burger numbers. This is due to the fact that, for low  $Bu$  values, the coherent structures appearing downstream are largely variable in amplitude and in space.

### 3.3 Form drag

The drag associated to pressure differences across an obstacle can be much larger than the frictional drag and represent the dominant mechanism to decelerate the coastal flow impinging on an obstacle (Moum and Nash, 2000; MacCready and Pawlak, 2001; Edwards et al., 2004; Klymak and Gregg, 2004). Changes in the momentum can result from skin friction as well as from the form drag associated to these differences (Baines, 1995; Kundu and Cohen, 2002). In this section of the paper, we want to quantify and compare form and frictional drags and to assess which physical processes are the cause for their different values in the various simulations.



If the sea surface height and the bottom surface are respectively at  $z = \eta(x, y, t)$  and at  $z = b(x, y)$ ,  $\rho$  the density field,  $\rho_0$  a constant background density,  $\rho' = \rho - \rho_0$ , and  $g$  the gravitational acceleration, the internal pressure associated with the deformation of the isopycnals upstream and downstream the cape can be calculated as  $p_{int}(x, y, t) = \int_b^\eta g \rho' dz$  (McCabe et al., 2006). We can then assume the pressure to be hydrostatic and split the contribution due to the sea surface elevation from the one due to  $p_{int}$ . Following the literature, these two different contributions are referred as external and internal form drags, respectively.

We normalize the drag forces for the different simulations using the characteristic velocity  $U$ , the density  $\rho_0$  and a suitable area. For the form drags, the projected frontal area of the obstacle  $A_{front}^{proj}$  is used, while, for the effective skin bottom drag, we use the surface of contact  $A_{cont}$  on which the bottom stress can act. This non-dimensionalization allows a comparison of the results in terms of the magnitude of the commonly used drag coefficient. The following expressions are therefore used:

$$C_{D_{Fric}}^{Eff}(t) = \frac{1}{\rho_0 U^2 A_{cont}} \int_{y_1}^{y_2} \int_{x_1}^{x_2} \tau_b^x(x, y, t) dx dy, \quad (1a)$$

$$C_{D_{Form}}^{Ext}(t) = \frac{1}{\rho_0 U^2 A_{front}^{proj}} \int_{y_1}^{y_2} \int_{x_1}^{x_2} -\rho_0 g \eta(x, y, t) \frac{\partial b}{\partial x} dx dy, \quad (1b)$$

$$C_{D_{Form}}^{Int}(t) = \frac{1}{\rho_0 U^2 A_{front}^{proj}} \int_{y_1}^{y_2} \int_{x_1}^{x_2} -p_{int}(x, y, t) \frac{\partial b}{\partial x} dx dy, \quad (1c)$$

$$C_{D_{Form}}^{Tot}(t) = C_{D_{Form}}^{Int}(t) + C_{D_{Form}}^{Ext}(t), \quad (1d)$$

where  $\tau_b^x$  is the along-shore component of the skin bottom friction stress. The double integral is performed on the area IJKL shown in Fig. 1. Specifically  $\overline{IJ} = x_2 - x_1$  and  $\overline{KJ} = y_2 - y_1$ .

The external form drag is expected to reflect all the sea surface deformations and to be associated with the eddies forming downstream of the cape over the area with slope topography. If we consider just the external contribution, lee cyclones will depress the sea surface enhancing the external pressure difference across the obstacle and increasing the form drag. For the same mechanism, anticyclones will elevate the surface decreasing the form drag. Given the sequence of anticyclones and cyclones, it is not exactly clear what the net external form drag will be in the case of eddy shedding.

The internal form drag, instead, is expected to be connected with the deep-

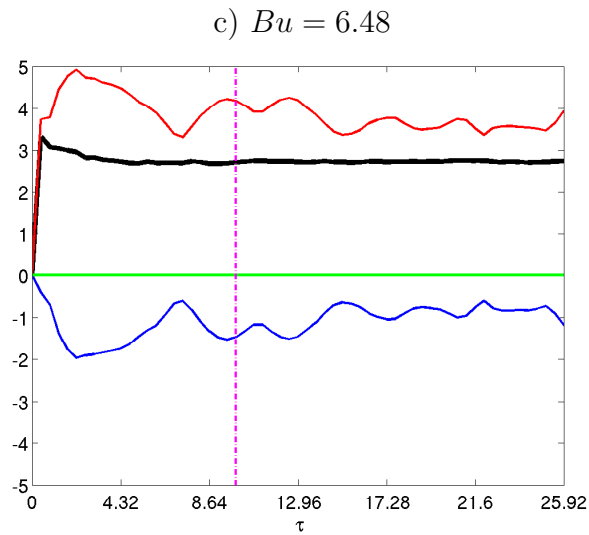
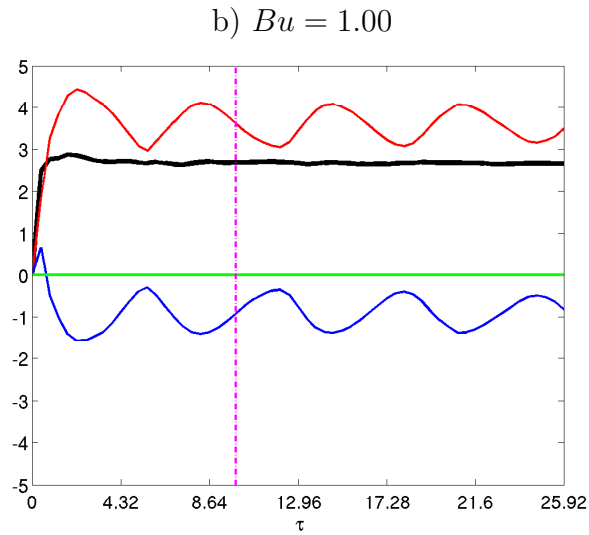
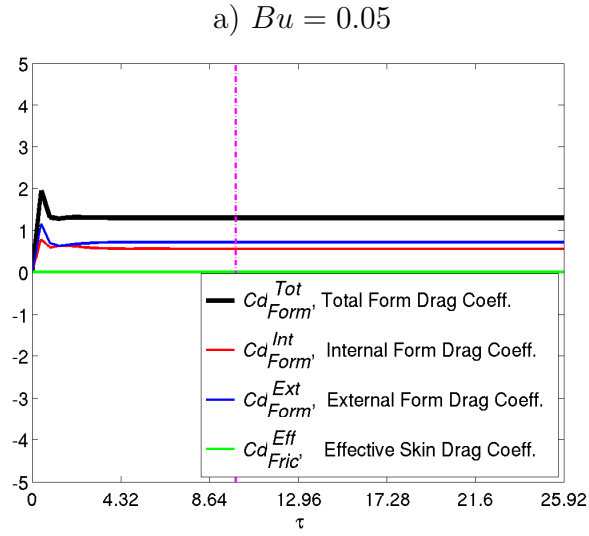


Fig. 11. Drag coefficients in time for the  $\alpha = 0.01$  simulations. The magenta dot-dashed vertical line indicates the specific time for Fig. 13.

ening of the isopycnals behind the ridge of the obstacle. This effect is usually due to the formation of lee waves (MacCready and Pawlak, 2001), but it can be also associated with the internal density structure of the eddies formed and shed. Also in this case, it is not clear what the net internal form drag will be when lee waves and different eddies coexist.

Fig. 11 shows the different drag coefficients calculated according to equations (1) for the  $\alpha = 0.01$  case and different  $Bu$ . In all cases the total form drag has the expected positive sign, i.e. it is directed opposite to the incoming current and it is much larger than the skin drag. A closer look at  $C_{D\text{ Fric}}^{Eff}$  reveals that this latter is always  $\mathcal{O}(10^{-3})$ , while for the  $\alpha = 0.01$  slope, the total form drag coefficient is always at least two orders of magnitude larger. When  $Bu = 0.05$  we know that no separation occurs. Thus, the external and the internal drags are both positive and stationary in time after an initial transient adjustment (Fig. 11a). Their addition results in a more positive total form drag. When  $Bu = 1.00$ , instead, external and internal drags are antisymmetric and regularly oscillating in time (Fig. 11b). The net result of such an asymmetry is a compensation which reduces the time variability of total form drag keeping it almost constant for all the simulated times (Fig. 11b). When  $Bu = 6.48$ , the form drags oscillate less regularly (Fig. 11c). They are always antisymmetric but larger than before. For this reason, the total form drag reaches a slightly more positive value than for  $Bu = 1.00$ .

Since the total form drag remains nearly constant after a short adjustment, we calculate a time average total form drag coefficient  $\langle C_{D\text{ Form}}^{Tot} \rangle$  for all the simulations. We decide to start from  $\tau = 4.32$  in order to exclude the transient adjustment period. In Fig. 12 the averaged total form drag coefficient  $\langle C_{D\text{ Form}}^{Tot} \rangle$  is reported on a semi-logarithmic plot in function of the Burger number and for different slopes. If we start the analysis with the  $\alpha = 1$  runs (blue crosses), we can see how the total amount of energy extracted from the large scale flow is clearly a function of the stratification. On a semi-logarithmic plot, such an increase is almost linear for small and intermediate Burger numbers, while it seems to slightly flatten out for higher  $Bu$ . The amount of energy extracted in the strongly stratified cases is much larger. For example, the total form drag coefficients for  $Bu = 6.48$  is  $\approx 1.75$ , i.e. almost seven times bigger than the  $Bu = 0.05$  case ( $\approx 0.25$ ). The same trend is found for different slopes: the total form drag always increases with  $Bu$ , for constant slopes. A general tendency to have flatter curves for high values of  $Bu$  can also be observed for gentler slope cases. However, the same coefficients are also systematically higher for decreasing slopes. This happens for all  $Bu$  and represents a surprising result, since the increase in drag moving toward gentler slopes is comparable to the one due to stronger stratification. For  $Bu = 0.05$ , for example, the total form drag coefficient for the  $\alpha = 0.005$  case is  $\approx 2$ , i.e. eight times bigger than for the  $\alpha = 1$  case.

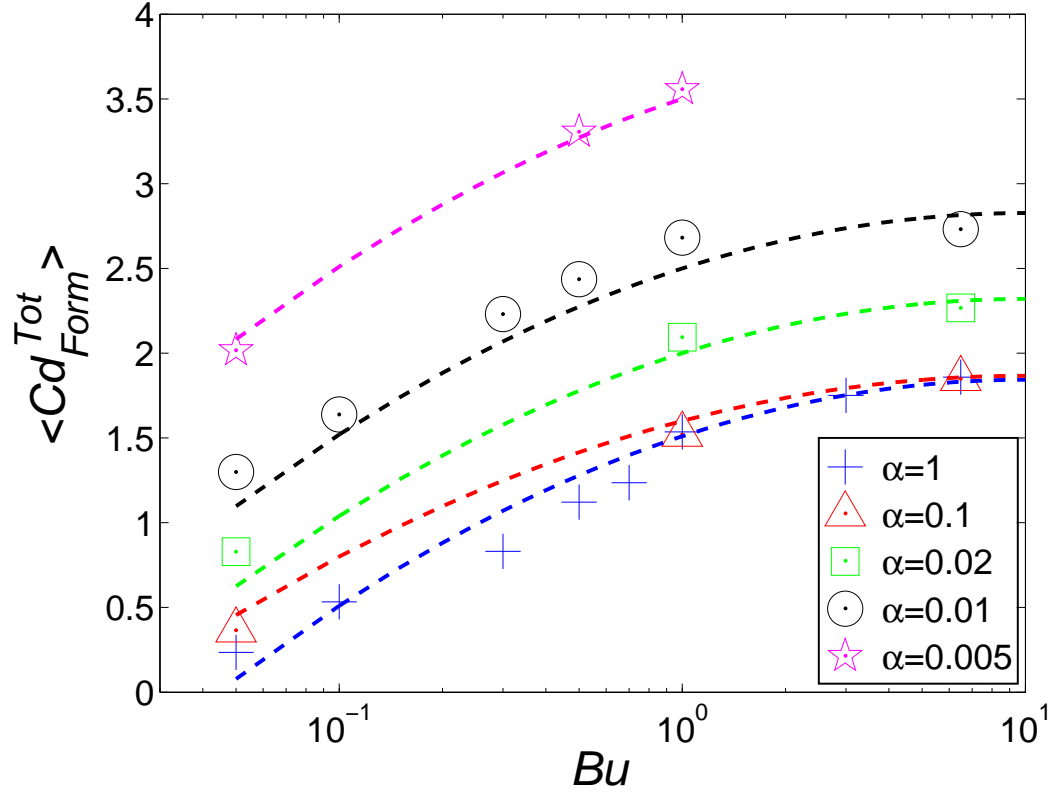


Fig. 12. Total Drag coefficients as a function of  $Bu$  and  $\alpha$ . Symbols refer to experiments and dashed lines are from equation (2). Note that the  $x$ -axis is logarithmic.

In order to derive a function able to parameterize the loss of momentum due to unresolved cape-like features in future coarse simulations, we fit empirically the dependency of the averaged total form drag coefficient on the Burger number and on the slope  $\alpha$ . For this purpose, the following second order logarithmic polynomial is proposed:

$$\langle C_{D_{Form}}^{Tot} \rangle (Bu, \alpha) = c_2(\alpha) \log^2(Bu) + c_1(\alpha) \log(Bu) + c_0(\alpha), \quad (2)$$

where, if  $m = 1/100$  and  $q = 1.5$ , the slope dependent constants are defined as:

$$\begin{aligned} c_0(\alpha) &= \frac{m}{\alpha} + q, \\ c_1(\alpha) &= -2c_2, \\ c_2(\alpha) &= -\left| \frac{1 - 2\alpha}{3} \right|. \end{aligned}$$

In Fig. 12 we graph with dashed lines the curves obtained using equation (2) for different Burger numbers and slopes. Fig. 12 and equation (2) empirically show

that the coastal flow experiences a larger drag for more stratified flows over gentler obstacles, but they do not explain what are the physical mechanisms behind this behavior. In particular we have to understand the reasons for:

- the oscillating antisymmetric patterns for external and internal form drags;
- the increase of the form drag for higher  $Bu$ , no matter what slope is considered;
- the increase of the form drag for gentler slopes, either for small or high  $Bu$ .

Let us consider five different quantities defined as

$$I(x, y, t) = \begin{cases} p_{int}(x, y, t) - p_{int}(x, y, t = 0) & \text{if } \frac{\partial b}{\partial x} \neq 0, \\ 0 & \text{if } \frac{\partial b}{\partial x} = 0, \end{cases} \quad (3)$$

$$E(x, y, t) = \begin{cases} \rho_0 g \eta(x, y, t) & \text{if } \frac{\partial b}{\partial x} \neq 0, \\ 0 & \text{if } \frac{\partial b}{\partial x} = 0, \end{cases} \quad (4)$$

$$S_I(y, t) = \frac{y_2 - y_1}{\rho_0 U^2 A_{front}^{proj}} \int_{x_1}^{x_2} -p_{int}(x, y, t) \frac{\partial b}{\partial x} dx, \quad (5)$$

$$S_E(y, t) = \frac{y_2 - y_1}{\rho_0 U^2 A_{front}^{proj}} \int_{x_1}^{x_2} -\rho_0 g \eta(x, y, t) \frac{\partial b}{\partial x} dx, \quad (6)$$

$$S_T(y, t) = S_I(y, t) + S_E(y, t). \quad (7)$$

The quantity  $I$  is the internal pressure field on the sea bottom subtracted at any time by the initial pressure and masked for null slope regions. Because of the along-stream symmetry of the obstacle in our simulations, the simultaneous presence of upstream positive and downstream negative anomalies is an indication of higher positive values for the internal form drag. The quantity  $E$ , instead, just masks the sea surface heights for null slope grid points and the differences across the obstacle of this quantity lead to different values for the external form drag. This difference reflects the variations of the sea surface for different mechanisms including the presence of different eddies in the lee of the cape. The quantities  $S_I$  and  $S_E$  sum up all the along-shore contributions to the internal and external form drag coefficients, respectively.  $S_T$  is just their net. They indicate where  $C_{D\ Form}^{Int}$  and  $C_{D\ Form}^{Ext}$  assume high values in the cross-stream direction. Looking at  $I$ ,  $E$ ,  $S_T$ ,  $S_I$  and  $S_E$ , we can basically establish where the highest contributions to the total, internal and external form drags take place.

Fig. 13 shows the plan view of  $I$  and  $E$  and the integrated quantities  $S_T$  (black thin line),  $S_I$  (red line) and  $S_E$  (blue line) for the same simulations

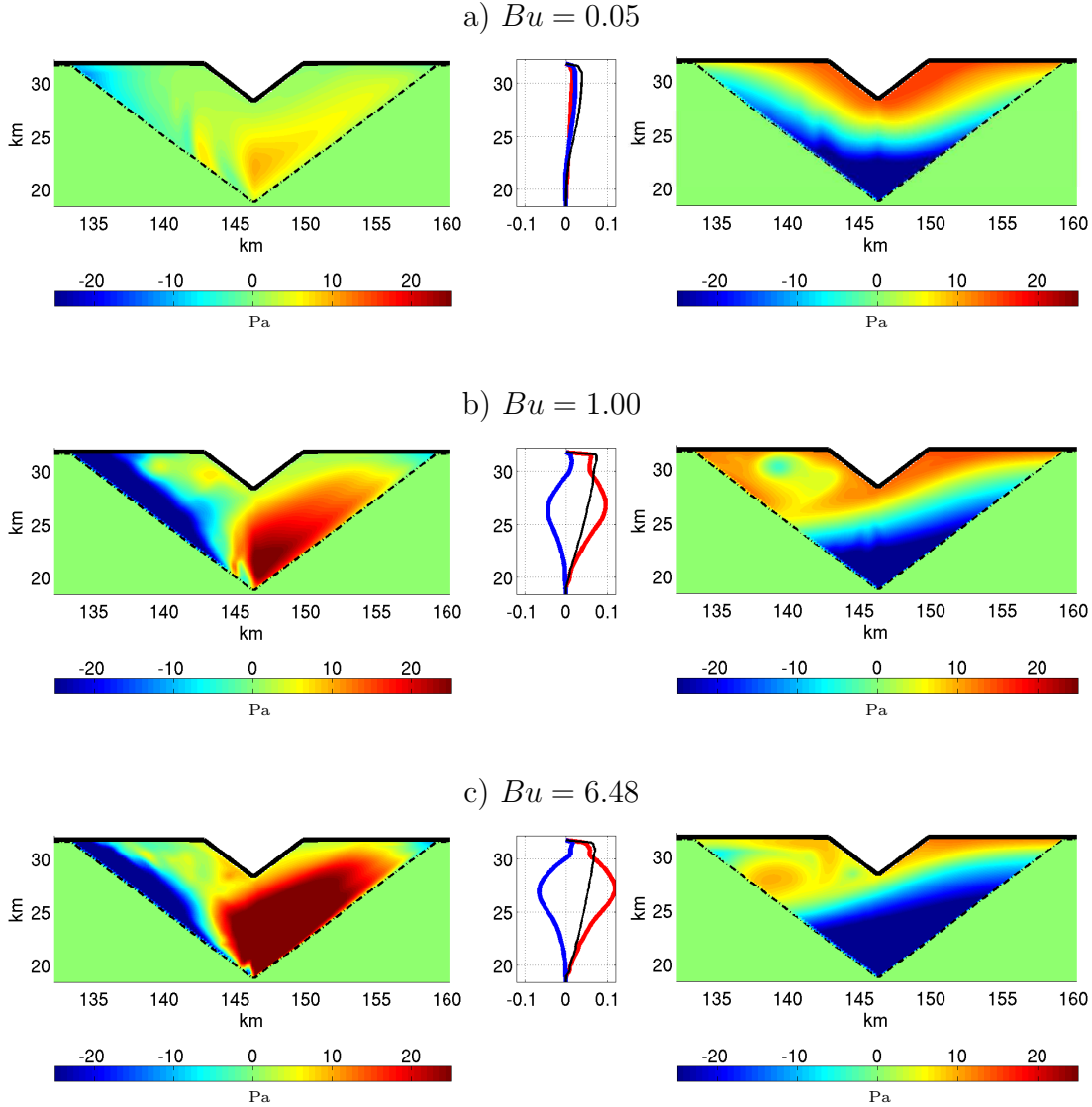


Fig. 13. Left panels: plan view of the quantity  $I$ . Center panels: the non-dimensional along-shore integrated quantities  $S_T$  (black thin line),  $S_I$  (red line) and  $S_E$  (blue line) as a function of the across-shore direction. Right panels: plan view of the quantity  $E$ . In all the plots  $\alpha = 0.01$ ,  $\tau = 9.936$  and the dash-dotted line indicates where the slope ends.

of Fig. 11, i.e. for  $\alpha = 0.01$  and for different  $Bu$ . In all the plots  $\tau = 9.936$  and the quantities reflect the situation of the vorticity fields shown in Fig. 6. Since we already know that the total form drag remains almost constant in time, the situation pictured in Fig. 13 can provide useful indications for the whole simulated time. The increase of the total form drag for higher  $Bu$  when  $\alpha$  is kept constant reflects the role of stratification in enhancing hori-

zonal movements and in favoring flow separation. When no separation occurs (Fig. 13a), both the internal pressure and the sea surface fields remain almost symmetric across the obstacle and the total form drag is positive but small. For increasing  $Bu$  (Fig. 13b), the separation process represents the common physical phenomenon leading to two diametrically opposite effects. It elevates the sea surface and depresses the isopycnals in the lee of the cape. This explain the clear antisymmetric temporal trends for internal and external drags. The level of the total drag is decided by the net of the two. When  $Bu = 6.48$ , the separation process is stronger and the drags are larger in magnitude but still oppositely directed. The net drag just increases slightly. This general scenario is complicated by the simultaneous surface eddy shedding regime at surface. When surface cyclones are formed (Fig. 13b), the sea surface locally depresses and the external form drag is less negative. Meanwhile the internal pressure difference and the internal form drag decrease. Viceversa for surface anticyclones. The eddies shedding at the surface are therefore responsible for the oscillations in the drag observed in time in Fig. 11b and 11c.

We now investigate the mechanism behind the increasing drag with gentler slopes. Since the separation process takes places also at intermediate or high  $Bu$ , it is likely that an explanation similar to the previous case can be found. Indeed, negative internal pressure areas appear downstream the obstacle and gradually increase in size for the gentler slope cases (not shown). Their preferential orientation is parallel to the obstacle baseline as before. We already know from the previous paragraph that in gentler slope cases larger eddies form and they are proportionally more in contact with the bottom than for steeper obstacles. Boundary layer mixing is therefore larger for decreasing slopes and the presence of lighter waters is responsible for the negative pressure anomalies downstream of the cape.

We still need to explain the mechanisms behind the increasing drag with gentler slopes for low  $Bu$ . In these cases, separation is not observed and the previous arguments do not work. Since all the simulations run at  $Bu = 0.05$  reach quickly a steady state, the situation depicted in the following figures for  $\tau = 9.936$  is representative of the whole simulation. Fig. 14 shows that negative internal pressure anomalies located in the area closer to the shore become gradually more important for gentler slope cases and are responsible for the increase of the internal form drag. Note that their preferential orientation is perpendicular to the obstacle baseline and not parallel as before. At the same time, a lee depression in the surface height located in the near-shore lee of the cape is responsible for the increase of the external form drag. Contrarily to what happens for larger  $Bu$ , the external form drag is now positive and it sums up with the internal for larger total drags values. In the last plot  $S_T$  is so big as to be off-scale.

In order to find a phenomenon able to explain the simultaneous appearance

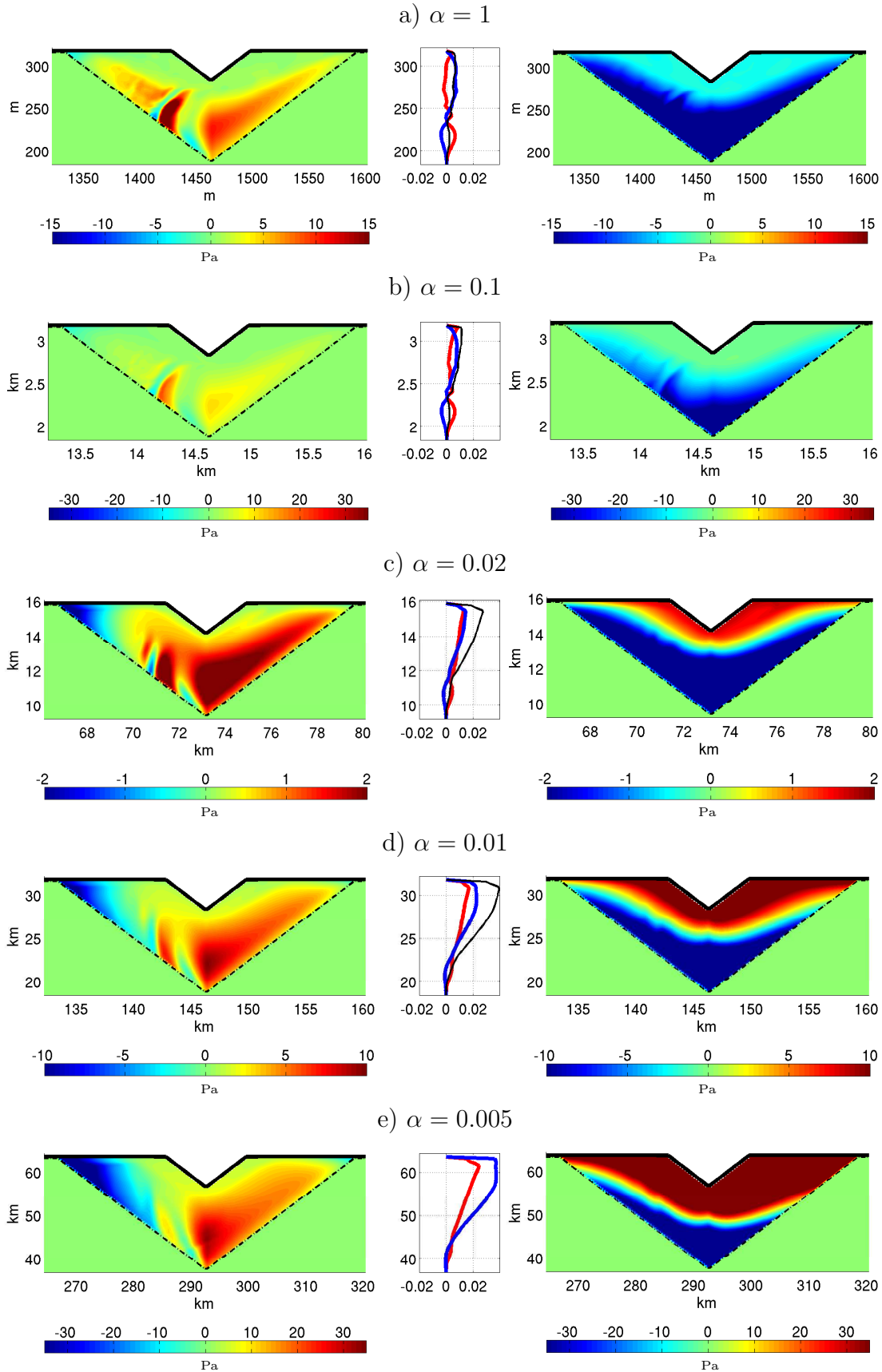
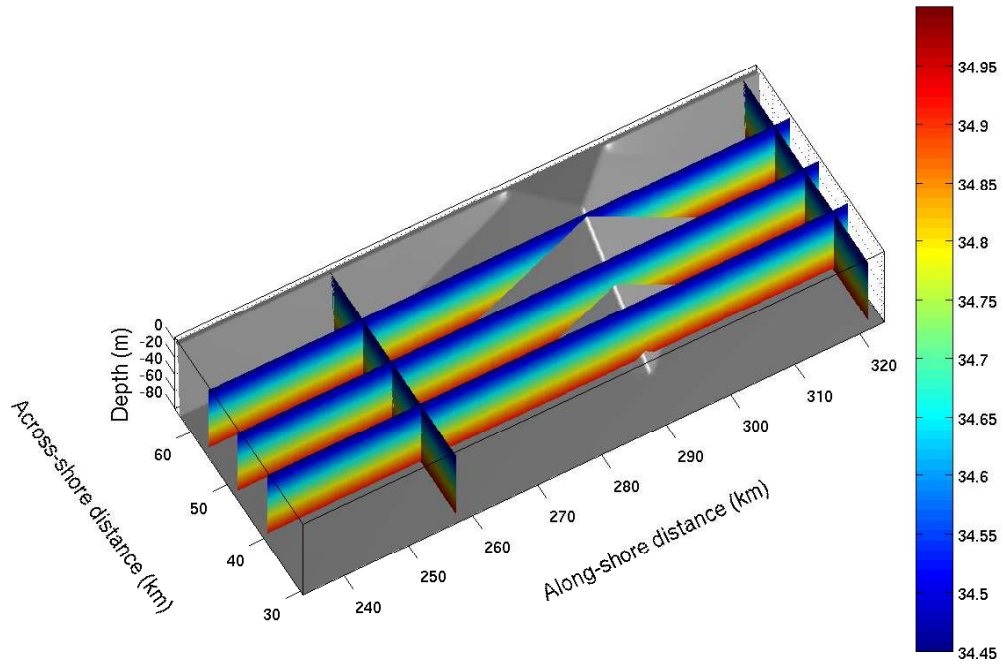


Fig. 14. As in Fig. 13 but for  $Bu = 0.05$  and different  $\alpha$ .



a)  $\tau = 0$



b)  $\tau = 9.936$

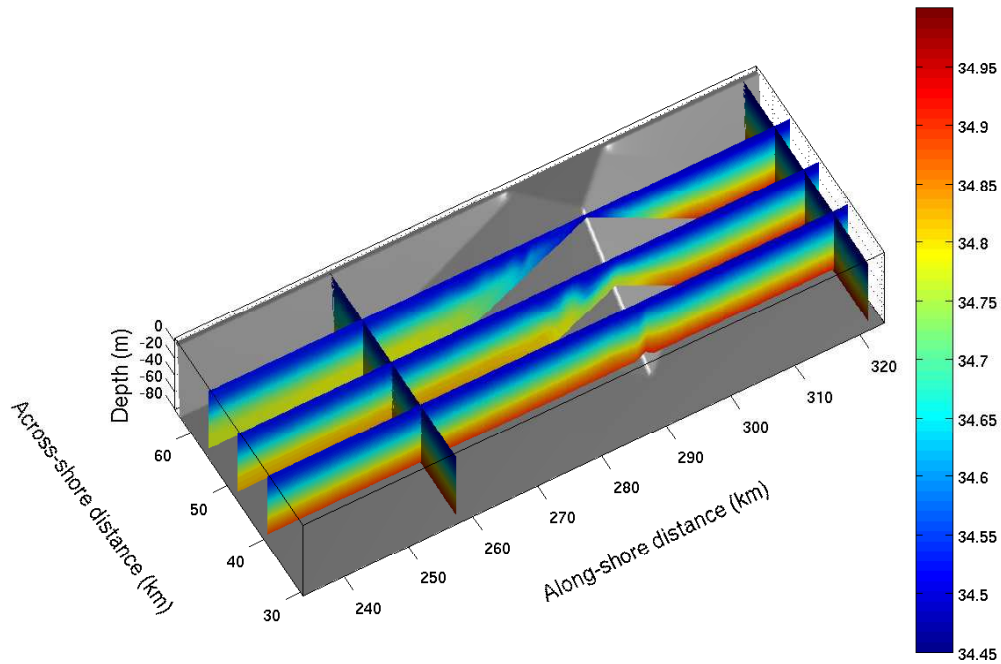


Fig. 15. Three-dimensional close up of the salinity field at different times for the case when  $Bu = 0.05$  and  $\alpha = 0.005$ .

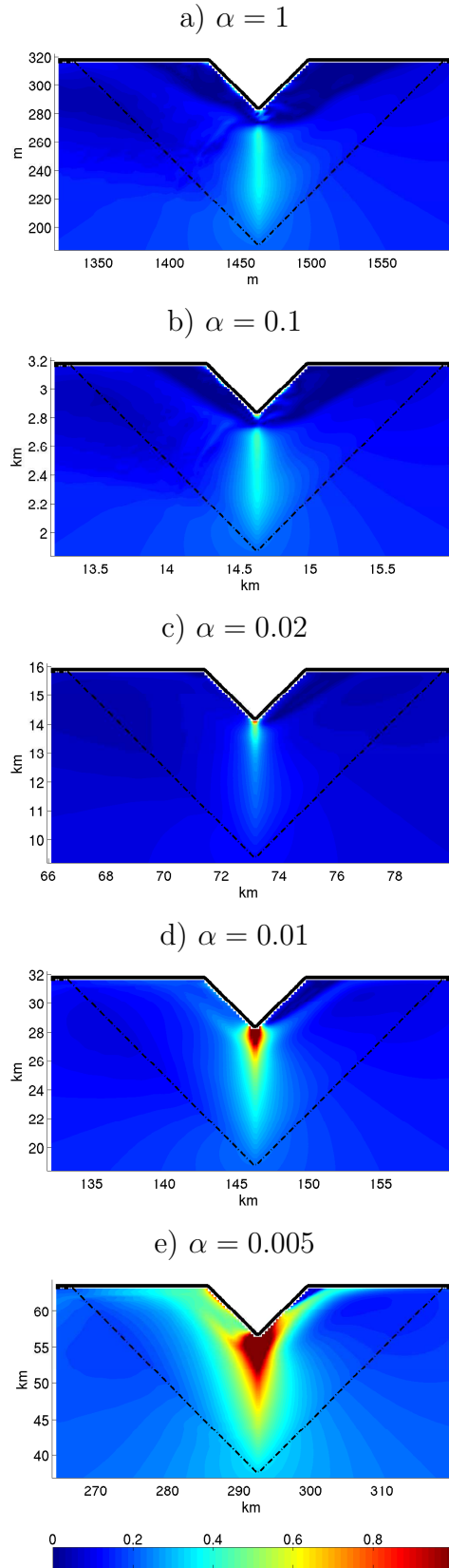


Fig. 16. Plan views of the local internal Froude numbers for the simulations with  $Bu = 0.05$  and different  $\alpha$ . In all the plots  $\tau = 9.936$  and the dotted line indicates where the slope ends.

of lighter water and surface depression in the lee of the cape, we also plot a three-dimensional view of the salinity field in the  $\alpha = 0.005$  case (Fig. 15). The initial condition is symmetric across the cape and does not result in a drag (Fig. 15a). However, if we look at the same field later on, the situation changes drastically. Near the coastline downstream of the cape, saltier waters are not present anymore. It is evident that the presence of lighter waters is linked to the increase in the ridge height moving toward the coast. Saltier waters are still retained offshore when the obstacle height is small but they gradually disappear close to the coast for increasing obstacle heights (Fig. 15b).

All the evidence collected so far suggests that the low  $Bu$  cases are dominated by hydraulic processes whose importance increases for gentler slopes. In order to confirm this hypothesis, the local internal Froude number is calculated in each grid-point according to the relation

$$Fr_I(x, y, t) = \frac{|\bar{u}(x, y, t)|}{\sqrt{g'(x, y, t) h(x, y, t)}}, \quad (8)$$

where  $\bar{u}$  is the along-shore component of the vertically averaged velocity,  $h$  is the depth and  $g' = g(\rho_{bot} - \rho_{surf})/\rho_0$  is the reduced gravity in each grid-point.  $\rho_{bot}$  and  $\rho_{surf}$  are the density values at the bottom and at the surface, respectively. Plan views of  $Fr_I$  for all the  $Bu = 0.05$  cases are shown in Fig. 16 for different slopes.  $Fr_I$  reaches the maximum in all the simulations at the crest of the ridge. Note that for gentler slope cases, the background flow increases by construction in order to keep constant the Rossby number (see Table 3). As a result, the extension of the area where the flow is supercritical increases as well. Supercritical conditions lead to a larger downstream mixing associated with hydraulic jumps. This mixing, the deepening of the sea surface height and of the isopycnals, all result in less bottom pressure on the lee-side of the cape and in a larger form drag.

#### 4 Summary and concluding remarks

We present a numerical study aimed to assess under which conditions different flow regimes occur behind a costal cape. We initially model after the laboratory experiments by Boyer and Tao (1987). As in the laboratory, if we keep constant the Rossby number, we observe that the regimes strongly depend on the Burger number  $Bu$ . For strongly stratified waters,  $Bu$  increases and horizontal movements are favored with respect to vertical ones. As a consequence, eddy separation is more likely to occur than lee wave generation and we pass from a fully-attached regime, to tip eddies, followed by a lee eddy shedding regime. For high  $Bu$  the lee shedding become stronger and more evident. The eddy-attached regime observed by Boyer and Tao (1987) for intermediate  $Bu$

is not reproduced in our simulations. We raise the possibility that this regime could be a very transient one, limited to a small parameter range between the fully-attached and the eddy shedding. Its relative importance in the laboratory experiments can be attributed to the smaller Reynolds numbers used.

The extension of the case study by [Boyer and Tao \(1987\)](#) to gentler and more realistic slopes reveals the competitive role of bottom friction. Bottom friction quickly damps and spins down turbulent structures while stratification tends to increase the two-dimensionality of the flow and to confine the damping role just to the deeper layers. For decreasing  $Re_f$  and slopes, the surface lee eddy shedding regime is gradually reached at higher  $Bu$ . For the gentler slope cases and for intermediate  $Bu$ , the regime is replaced by just tip eddies. At the bottom, the strong lee eddy shedding is weakened for intermediate slope. For gentler slope cases, bottom friction becomes so important as to slow down the eddy formation. It can spin down the first eddy forming in the lee (eddy-attached regime) or to inhibit completely its formation. In the latter case, only tip eddies can be observed. Flow diagram regimes summarizing these results are presented. Finally, when the lee eddy shedding regime is established, the Strouhal number is shown to decrease with the Burger number.

Even if bottom friction plays a key role in setting up the flow regimes behind the cape, the quantification of the form drag coefficients in all the simulations shows that these latter are at least  $\mathcal{O}(10^{-1})$ , i.e. 100 times bigger than the skin drag ones. This result is consistent with previous works recognizing the form drag as the principal mechanism for the loss of momentum in a coastal flow ([Moum and Nash, 2000](#); [MacCready and Pawlak, 2001](#); [Klymak and Gregg, 2004](#)). However, it should be noted that the ratio of form drag to skin friction scales somewhat as the ratio of the relative drag coefficients multiplied by the aspect ratio. The total form drag therefore is almost 20 times larger than skin friction for  $\alpha = 1$ , but of the same order of magnitude for  $\alpha = 0.005$ .

In order to understand which physical processes are responsible of the form drag values, we tell apart the two different contributions due to sea surface anomalies and to isopycnal deformations. The internal and external form drag coefficients are calculated separately and then summed up. We found that in weakly stratified non-eddy regimes, the internal and external form drags are due to internal waves and both are positive. When the flow is subcritical (steep cases), their values are small, but in the presence of supercritical flows with hydraulic jumps (gentle cases), the downstream mixing, the deepening of the isopycnals and of the sea surface are so substantial as to result in larger drag values. When the stratification increases, the external form drag is positive and it opposes the deceleration of the flow. This is due to the predominant presence of positive sea surface anomalies associated with the separation process behind the cape. The respective internal structure, however, leads to the opposite effect for the internal pressure at the bottom. As a result,

the internal form drag shows an antisymmetric temporal trend relative to the external drag, and it is able to overcome the latter. The increasing tendency for flow separation and eddy generation for higher  $Bu$  and gentler slopes sets up the mean level drag values and leads to larger form drag coefficients. The surface eddy shedding is merely responsible for the oscillating time pattern around this level.

The results presented, therefore, provide useful insights for future and more realistic modeling. Here we underline how the form drag strongly depends on the flow regimes and on the physical processes established in different conditions. Moreover, the scientific literature already recognizes the importance of the form drag in explaining strong additional dissipation in coastal areas rich with topographic features (Lavelle et al., 1988; Foreman et al., 1995; Edwards et al., 2004). In order to simulate the effects of unresolved capes in future simulations, we put forth an empirical fit to the form drag coefficient in the  $Bu - \alpha$  space based on the numerical experiments. The proposed function can be employed as a parametrization of form drag associated with flows past unresolved capes in coarse resolution simulations.

This study has also implications for the transport of pollutants, sediments and biological substances. The results indicate that larger particle trapping by the eddies and consequent dispersion when they shed, are phenomena likely to occur for steeper capes and in summertime, when waters are less affected by bottom friction and more stratified. At the same time, for the gentler slope cases, this study shows that horizontal dispersion at the bottom is strongly reduced when the eddy-attached regime occurs. If a pollutant source is located at depth in the lee of the cape (e.g. sewage pipes), these results suggest that anoxic conditions are more likely to occur.

The results here presented are limited to the  $Ro = 0.06$  case. The mechanism for the vorticity generation is not assessed in this study and the approach followed in Signell and Geyer (1991) and in Dong and McWilliams (2007) looks promising. More work is needed to assess this point and the sensitivity to the Rossby number. Moreover, the conclusions of the study are strongly related to the geometry of the cape. Its horizontal dimension, its slope and the shape of the submerged ridge are shown to influence the results throughout the paper. The actual generalization of the phenomena here described is not yet assessed at this stage. There are many effects that can contribute to alter the flow dynamics and the form drag, such as the variability of the incoming current (Aiken et al., 2002) or the direction and the strength of a blowing wind (Winant, 2006). Further investigations in terms of both numerical modeling and field measurements are necessary to assess all these points.

## Acknowledgements

We thank Mehmet Ilıcak and Andrea M. Doglioli for their constructive criticism in different phases of this study. The authors greatly appreciate discussions with Parker MacCready, Wayne R. Geyer and Peter G. Baines. We also thank two anonymous reviewers for improving the manuscript. This research was supported by the National Ocean Partnership Program. T. M. Özgökmen and A. Griffa were partially supported by ONR grants N00014-05-1-0094, N00014-05-1-0095.

## A Classification of flow regimes

The time evolution of the ratio  $KE/KE_0$  can be used to classify the different flow regimes in the numerical runs.

Tables [A.1](#) and [A.2](#) collect the trend types and the temporal standard deviations  $\sigma$  for each simulation at surface and at the bottom, respectively. For the calculation of  $\sigma$ , we start from  $\tau = 4.32$  to exclude the initial transient adjustment period. The flow regimes are assigned according to the type of trend and the value of  $\sigma$ . The type of trend is looked first. If it is an oscillating regime, the value of the standard deviation is considered. Specifically:

- if  $\sigma \leq 3 \times 10^{-2}$   $\mapsto$  Tip eddies regime;
- if  $3 \times 10^{-2} < \sigma \leq 1 \times 10^{-1}$   $\mapsto$  Lee eddy shedding regime;
- if  $\sigma > 1 \times 10^{-1}$   $\mapsto$  Strong lee eddy shedding regime.

If it is a decaying trend, a second decision is taken based on  $\sigma$ . If  $\sigma > 1 \times 10^{-1}$  the strong energetic shedding is just weakened, while if  $\sigma \leq 1 \times 10^{-1}$ , an eddy-attached regime is assigned. Finally, if it is a flat and steady trend, a fully-attached regime is assigned.

The information contained in Tables [A.1](#) and [A.2](#) are displayed in the already proposed Fig. [8](#).

<i>Surface</i>					
Exp.	$Re_f (\alpha)$	$Bu$	Trend	$\sigma$	Regime
2	208 (1)	0.05	Steady	$3.50 \times 10^{-3}$	Fully-attached
3	208 (1)	0.10	Oscillating	$7.00 \times 10^{-3}$	Tip eddies
4	208 (1)	0.30	Oscillating	$1.87 \times 10^{-2}$	Tip eddies
5	208 (1)	0.50	Oscillating	$7.35 \times 10^{-2}$	Eddy shedding
6	208 (1)	0.70	Oscillating	$6.67 \times 10^{-2}$	Eddy shedding
7	208 (1)	1.00	Oscillating	$8.78 \times 10^{-2}$	Eddy shedding
8	208 (1)	3.00	Oscillating	$1.54 \times 10^{-1}$	Strong eddy shedding
9	208 (1)	6.48	Oscillating	$1.30 \times 10^{-1}$	Strong eddy shedding
10	21 (0.1)	0.05	Steady	$2.22 \times 10^{-3}$	Fully-attached
11	21 (0.1)	1.00	Oscillating	$6.17 \times 10^{-2}$	Eddy shedding
12	21 (0.1)	6.48	Oscillating	$1.65 \times 10^{-1}$	Strong eddy shedding
13	4 (0.02)	0.05	Steady	$3.61 \times 10^{-4}$	Fully-attached
14	4 (0.02)	1.00	Oscillating	$7.20 \times 10^{-2}$	Eddy shedding
15	4 (0.02)	6.48	Oscillating	$2.61 \times 10^{-1}$	Strong eddy shedding
16	2 (0.01)	0.05	Steady	$1.85 \times 10^{-4}$	Fully-attached
17	2 (0.01)	0.10	Steady	$9.02 \times 10^{-5}$	Fully-attached
18	2 (0.01)	0.30	Oscillating	$1.29 \times 10^{-2}$	Tip eddies
19	2 (0.01)	0.50	Oscillating	$1.47 \times 10^{-2}$	Tip eddies
20	2 (0.01)	1.00	Oscillating	$4.89 \times 10^{-2}$	Eddy shedding
21	2 (0.01)	6.48	Oscillating	$1.47 \times 10^{-1}$	Strong eddy shedding
22	1 (0.005)	0.05	Steady	$1.58 \times 10^{-4}$	Fully-attached
23	1 (0.005)	0.50	Oscillating	$6.85 \times 10^{-3}$	Tip eddies
24	1 (0.005)	1.00	Oscillating	$3.92 \times 10^{-2}$	Eddy shedding

Table A.1  
Classification of surface flow regimes for all the simulations.

<i>Bottom</i>					
Exp.	$Re_f (\alpha)$	$Bu$	Trend	$\sigma$	Regime
2	208 (1)	0.05	Steady	$4.49 \times 10^{-3}$	Fully-attached
3	208 (1)	0.10	Oscillating	$8.75 \times 10^{-3}$	Tip eddies
4	208 (1)	0.30	Oscillating	$5.19 \times 10^{-2}$	Eddy shedding
5	208 (1)	0.50	Oscillating	$1.11 \times 10^{-1}$	Strong eddy shedding
6	208 (1)	0.70	Oscillating	$1.90 \times 10^{-1}$	Strong eddy shedding
7	208 (1)	1.00	Oscillating	$2.15 \times 10^{-1}$	Strong eddy shedding
8	208 (1)	3.00	Oscillating	$4.71 \times 10^{-1}$	Strong eddy shedding
9	208 (1)	6.48	Oscillating	$5.11 \times 10^{-1}$	Strong eddy shedding
10	21 (0.1)	0.05	Steady	$3.34 \times 10^{-3}$	Fully-attached
11	21 (0.1)	1.00	Decaying	$1.63 \times 10^{-1}$	Eddy shedding
12	21 (0.1)	6.48	Decaying	$2.86 \times 10^{-1}$	Eddy shedding
13	4 (0.02)	0.05	Steady	$1.03 \times 10^{-4}$	Fully-attached
14	4 (0.02)	1.00	Decaying	$3.20 \times 10^{-2}$	Eddy-attached
15	4 (0.02)	6.48	Decaying	$5.91 \times 10^{-2}$	Eddy-attached
16	2 (0.01)	0.05	Steady	$8.10 \times 10^{-5}$	Fully-attached
17	2 (0.01)	0.10	Steady	$1.62 \times 10^{-4}$	Fully-attached
18	2 (0.01)	0.30	Oscillating	$7.19 \times 10^{-3}$	Tip eddies
19	2 (0.01)	0.50	Oscillating	$1.48 \times 10^{-2}$	Tip eddies
20	2 (0.01)	1.00	Oscillating	$1.25 \times 10^{-2}$	Tip eddies
21	2 (0.01)	6.48	Decaying	$5.83 \times 10^{-2}$	Eddy-attached
22	1 (0.005)	0.05	Steady	$4.56 \times 10^{-5}$	Fully-attached
23	1 (0.005)	0.50	Oscillating	$3.14 \times 10^{-3}$	Tip eddies
24	1 (0.005)	1.00	Oscillating	$6.30 \times 10^{-3}$	Tip eddies

Table A.2  
Classification of bottom flow regimes for all the simulations.



## References

- Aiken, C. M., Moore, A. M., Middleton, J. H., 2002. The nonnormality of coastal ocean flows around obstacles and their response to stochastic forcing. *J. Mar. Sys.* 32 (10), 2955–2974.
- Armi, L., 1986. The hydraulics of two flowing layers with different densities. *J. Fluid Mech.* 163, 27–58.
- Armi, L., Farmer, D. M., 1986. Maximal two-layer exchange through a contraction with barotropic net flow. *J. Fluid Mech.* 164, 27–51.
- Baines, P. G., 1995. *Topographic Effects in Stratified Flows*. Cambridge University Press.
- Bastos, A., Collins, M., Kenyon, N., 2003. Water and sediment movement around a coastal headland: Portland Bill, Southern UK. *Ocean Dynamics* 53 (3), 309–321.
- Bastos, A., Kenyon, N., Collins, M., 2002. Sediment processes, bedforms and facies, associated with a coastal headland: Portland Bill, Southern UK. *Mar. Geol.* 187 (3-4), 235–258.
- Batchelor, G., 1967. *An Introduction to Fluid Dynamics*. Cambridge University Press.
- Boyer, D., Chen, R., d’Hières, G. C., Didelle, H., 1987. On the formation and shedding of vortices from side-wall mounted obstacles in rotating systems. *Dyn. Atmos. Oceans* 11, 59–86.
- Boyer, D., Davies, P. A., 1982. Flow past a cylinder on a  $\beta$ -plane. *Phil. Trans. R. Soc. London A* 306, 33–56.
- Boyer, D., Metz, M. L., 1983. Vortex shedding in rotating flows. *Geophys. Astrophys. Fluid Dynamics* 26, 51–83.
- Boyer, D., Tao, L., 1987. On the motion of linearly stratified rotating fluids past capes. *J. Fluid Mech.* 180, 429–449.
- Canuto, V. M., Howard, A., Cheng, Y., Dubovikov, M. S., 2001. Ocean turbulence, Part i: one-point closure model momentum and heat vertical diffusivities. *J. Phys. Oceanogr.* 31, 1413–1426.
- Chiswell, S., Roemmich, D., 1998. The East Cape Current and two eddies: a mechanism for larval retention? *N. Z. J. Mar. Freshwat. Res.* 32 (3), 385–397.
- Coutis, P. F., Middleton, J. H., 2002. The physical and biological impact of a small island wake in the deep ocean. *Deep Sea Res. I* 49, 1341–1361.
- Cushman-Roisin, B., Korotenko, K. A., Galos, C. E., Dietrich, D. E., 2007. Simulation and characterization of the Adriatic Sea mesoscale variability. *J. Geophys. Res.* 112, C03S14, doi:10.1029/2006JC003515.
- Davies, P. A., Besley, P., Boyer, D. L., 1990a. An experimental study of flow past a triangular cape in a linearly stratified fluid. *Dyn. Atmos. Oceans* 14 (6), 497–528.
- Davies, P. A., Dakin, J., Falconer, R., 1995. Eddy formation behind a coastal headland. *J. Coast. Res.* 11 (1), 154–167.
- Davies, P. A., Davis, R. G., Foster, M. R., 1990b. Flow past a cylinder in a

- rotating stratified fluid. *Phil. Trans. R. Soc. London A* 331, 245–286.
- Doglioli, A. M., Griffa, A., Magaldi, M. G., 2004a. Numerical study of a coastal current on a steep slope in presence of a cape: the case of the Promontorio di Portofino. *J. Geophys. Res.* 109, C12033, doi:10.1029/2004JC002422.
- Doglioli, A. M., Magaldi, M. G., Vezzulli, L., Tucci, S., 2004b. Development of a numerical model to study the dispersion of wastes coming from a marine fish farm in the Ligurian Sea (Western Mediterranean). *Aquaculture* 231 (1-4), 215–235, doi:10.1016/j.aquaculture.2003.09.030.
- Dong, C., McWilliams, J. C., 2007. A numerical study of island wakes in the Southern California Bight. *Cont. Shelf Res.* 27, 1233–1248.
- Dong, C., McWilliams, J. C., Shchepetkin, A. F., 2007. Island wakes in deep water. *J. Phys. Oceanogr.* 37, 962–981, doi:10.1175/JPO3047.1.
- Edwards, K. A., MacCready, P., Moum, J. N., Pawlak, G., 2004. Form drag and mixing due to tidal flow past a sharp point. *J. Phys. Oceanogr.* 34, 1297–1312.
- Farmer, D. M., Armi, L., 1986. Maximal two-layer exchange over a sill and through the combination of a sill and contraction with barotropic flow. *J. Fluid Mech.* 164, 53–76.
- Farmer, R., Pawlowicz, D., Jiang, R., 2002. Tilting separation flows: a mechanism for intense vertical mixing in the coastal ocean. *Dyn. Atmos. Oceans* 36, 43–58.
- Foreman, M. G. G., Walters, R. A., Henry, R. F., Keller, C. P., Dolling, A. G., 1995. A tidal model for eastern Juan de Fuca Strait and the southern Strait of Georgia. *J. Geophys. Res.* 100 (C1), 721–740.
- Freeland, H., 1990. The flow of a coastal current past a blunt headland. *Atmosphere-Ocean* 28, 288–302.
- Geyer, W. R., 1993. Three-dimensional tidal flow around headlands. *J. Geophys. Res.* 98 (C1), 955–966.
- Hayward, T. L., Mantyla, A. W., 1990. Physical, chemical and biological structure of a coastal eddy near Cape Mendocino. *J. Mar. Res.* 48, 825–850.
- Heywood, K. J., Stevens, D. P., Bigg, G. R., 1996. Eddy formation behind the tropical island of Aldabra. *Deep Sea Res. I* 43 (4), 555–578.
- John, M. A. S., Pond, S., 1992. Tidal plume generation around a promontory: effects on nutrient concentrations and primary productivity. *Cont. Shelf Res.* 12 (2-3), 339–354.
- Jones, O. P., Simons, R. R., Jones, E. J. W., Harris, J. M., 2006. Influence of seabed slope and Coriolis effects on the development of sandbanks near headlands. *J. Geophys. Res.* 111, C03020, doi:10.1029/2005JC002944.
- Klinger, B. A., 1993. Gyre formation at the corner by rotating barotropic coastal flows along a slope. *Dyn. Atmos. Oceans* 19, 27–64.
- Klymak, J. M., Gregg, M. C., 2001. Three-dimensional nature of flow near a sill. *J. Geophys. Res.* 106 (C10), 22295–22311.
- Klymak, J. M., Gregg, M. C., 2004. Tidally generated turbulence over the Knight Inlet Sill. *J. Phys. Oceanogr.* 34 (5), 1135–1151.
- Kundu, P. K., Cohen, I. M., 2002. *Fluid Mechanics*, 2nd Ed. Academic Press.

- Lavelle, J. W., Mofjeld, H. O., Lempriere-Doggett, E., Cannon, G. A., Pashinski, D. J., Cokelet, E. D., Lytle, L., Gill, S., 1988. A multiply-connected channel model of tides and tidal currents in Puget Sound, Washington and a comparison with updated observations. Technical Memorandum ERL PMEL-84, NOAA, 103pp.
- Lin, J. T., Pao, Y. H., 1979. Wakes in stratified fluids. *Ann. Rev. Fluid Mech.* 11, 317–338, doi:10.1146/annurev.fl.11.010179.001533.
- Lloyd, P. M., Stansby, P. K., Chen, D., 2001. Wake formation around islands in oscillatory laminar shallow water flows. Part I: Experimental investigation. *J. Fluid Mech.* 429, 217–238.
- MacCready, P., Pawlak, G., 2001. Stratified flow along a corrugated slope: separation drag and wave drag. *J. Phys. Oceanogr.* 31 (10), 2824–2839.
- McCabe, R. M., MacCready, P. M., Pawlak, G., 2006. Form drag due to flow separation at a headland. *J. Phys. Oceanogr.* 36 (11), 2136–2152.
- Merkine, L.-O., 1980. Flow separation on a  $\beta$ -plane. *J. Fluid Mech.* 99, 399–409.
- Merkine, L.-O., Solan, A., 1979. The separation of flow past a cylinder in a rotating system. *J. Fluid Mech.* 92, 381–392.
- Moum, J. N., Nash, J. D., 2000. Topographically induced drag and mixing at a small bank on the continental shelf. *J. Phys. Oceanogr.* 35 (8), 2049–2054.
- Murdoch, R. C., 1989. The effects of a headland eddy on surface macrozooplankton assemblages north of Ontago Peninsula, New Zealand. *Estuar. Coast. Shelf S.* 29, 361–383.
- Nash, J. D., Moum, J. N., 2001. Internal hydraulic flows on the continental shelf: high drag states over a small bank. *J. Geophys. Res.* 106 (C3), 4593–4611.
- Neill, S. P., Elliott, A. J., 2004. Observations and simulations of an unsteady island wake in the Firth of Forth, Scotland. *Ocean Dynamics* 54, 324–332.
- Page, M. A., 1985. On the low rossby number flow of a rotating fluid past a cylinder. *J. Fluid Mech.* 156, 205–211.
- Pattiaratchi, C., James, A., Collins, M., 1986. Island wakes and headland eddies: a comparison between remotely sensed data and laboratory experiments. *J. Geophys. Res.* 92 (C1), 783–794.
- Pawlak, G., Armi, L., 1996. Stability and mixing of a two-layer exchange flow. *Dyn. Atmos. Oceans* 24, 139–151, doi:10.1016/0377-0265(95)00447-5.
- Pawlak, G., Armi, L., 1997. Hydraulics of two-layer arrested wedge flows. *J. Hydr. Res.* 35 (5), 603–618.
- Pawlak, G., MacCready, P., Edwards, K. A., McCabe, R., 2003. Observations on the evolution of tidal vorticity at a stratified deep water headland. *Geophys. Res. Lett.* 30 (24), 2234, doi:10.1029/2001JC001234.
- Pedlosky, J., 1987. *Geophysical Fluid Dynamics*, 2nd Ed. Springer-Verlag.
- Pingree, R. D., 1978. The formation of the shambles and other banks by tidal stirring of the seas. *J. Mar. Biol. Ass. U.K.* 58, 211–226.
- Pingree, R. D., Maddock, L., 1980. The effects of bottom friction and Earth's rotation on an island's wake. *J. Mar. Biol. Ass. U.K.* 60, 499–508.

- Rankin, K. L., Mullineaux, L. S., Geyer, W. R., 1994. Transport of juvenile gem clams (*Gemma gemma*) in a headland wake. *Estuaries* 17 (3), 655–667.
- Roughan, M., Mace, J., Largier, J. L., Morgan, S. G., Fisher, J. L., Carter, M. L., 2005. Subsurface recirculation and larval retention in the lee of a small headland: a variation on the upwelling shadow theme. *J. Geophys. Res.* 110, C10027, doi:10.1029/2005JC002898.
- Schlichting, H., Gersten, K., 2003. *Boundary Layer Theory*. Springer-Verlag.
- Shchepetkin, A. F., McWilliams, J. C., 1998. Quasi-monotone advection schemes based on explicit locally adaptive dissipation. *Mon. Weather Rev.* 126 (6), 1541–1580.
- Shchepetkin, A. F., McWilliams, J. C., 2005. The regional oceanic modeling system (ROMS): a split-explicit, free-surface, topography-following-coordinate oceanic model. *Ocean Modell.* 9 (4), 347–404.
- Shchepetkin, A. F., O’Brien, J. J., 1996. A physically consistent formulation of lateral friction in shallow-water equation ocean models. *Mon. Weather Rev.* 124 (6), 1285–1300.
- Signell, R., Geyer, W., 1991. Transient eddy formation around headlands. *J. Geophys. Res.* 96 (C2), 2561–2575.
- Stansby, P. K., Lloyd, P. M., 2001. Wake formation around islands in oscillatory laminar shallow water flows. Part II: Three-dimensional boundary-layer modelling. *J. Fluid Mech.* 429, 217–238.
- Tansley, C., Marshall, D. P., 2001. Flow past a cylinder on a  $\beta$ -plane, with application to Gulf Stream separation and the Antarctic Circumpolar Current. *J. Phys. Oceanogr.* 31, 3274–3283.
- Tomczak, M., 1988. Island wakes in deep and shallow water. *J. Geophys. Res.* 93 (C5), 5153–5154.
- Umlauf, L., Burchard, H., 2003. A generic length-scale equation for geophysical turbulence models. *J. Marine Res.* 61, 235–265.
- Veneziani, M., Griffa, A., Poulain, P.-M., 2007. Historical drifter data and statistical prediction of particle motion: a case study in the central Adriatic Sea. *J. Atmos. Ocean. Tech.* 24, 235–254, doi:10.1175/JTECH1969.1.
- Verron, J., Davies, P. A., Dakin, J. M., 1991. Quasigeostrophic flow past a cape in a homogeneous fluid. *Fluid Dyn. Res.* 7, 1–21.
- Walker, J. D. A., Stewartson, K., 1972. The flow past a cylinder in a rotating frame. *Z. Angew. Math. Phys.* 23, 745–752.
- Winant, C. D., 2006. Three-dimensional wind-driven coastal circulation past a headland. *J. Phys. Oceanogr.* 36, 1430–1438.
- Wolanski, E., Asaeda, T., Tanaka, A., Deleersnijder, E., 1996. Three-dimensional island wakes in the field, laboratory experiments and numerical models. *Cont. Shelf Res.* 16 (11), 1437–1452.
- Wolanski, E., Imberger, J., Heron, M., 1984. Island wakes in shallow coastal waters. *J. Geophys. Res.* 89 (C6), 10553–10569.